Computer Methods in Applied Mechanics and Engineering 449 (2026) 118505

Contents lists available at ScienceDirect

Comput. Methods Appl. Mech. Engrg.

journal homepage: www.elsevier.com/locate/cma

A SPH multi-resolution framework for multi-phase flows

Niklas Bürkle [a,*], Markus Wicker [a], Max Okraschevski [b,c], Rainer Koch [a], Hans-Jörg Bauer [a]

[a] Institute of Thermal Turbomachinery, Karlsruhe Institute of Technology (KIT), Karlsruhe, Germany
[b] Institute of Engineering Thermodynamics, German Aerospace Center (DLR), Ulm, Germany
[c] Helmholtz Institute Ulm for Electrochemical Energy Storage (HIU), Ulm, Germany

ARTICLE INFO

Keywords:
Smoothed particle hydrodynamics (SPH)
Particle refinement
Multi-resolution
Adaptivity
Grand challenges
Multi-phase flows

ABSTRACT

Smoothed Particle Hydrodynamics (SPH) is a particle method frequently employed for the prediction of multi-phase flows in technical applications. The development of accurate and efficient multi-resolution SPH is considered a so-called Grand Challenge by the SPH community, and significant efforts have been made to address this issue. Unfortunately, especially for multi-phase flows, available approaches are scarce. This is due to another challenging aspect, the transport of a discontinuity inherent to this kind of flow: the phase interface. Up to now, no multi-resolution approach is available that is capable to transport and preserve this discontinuity across different resolution levels. To this end, a novel framework was developed that incorporates a domain-decomposition approach, a state-of-the-art particle generation and deletion algorithm, as well as a reconstruction of the phase interface at the internal boundary. The framework is applicable and tailored to multi-phase flows since it allows surface tension effects to be accounted for across different resolution levels. Its capabilities are evaluated by several benchmarks, proving good agreement to the reference results. Finally, the multi-resolution framework is demonstrated in an application-relevant atomizer case.

1. Introduction

In recent decades, Lagrangian methods such as Smoothed Particle Hydrodynamics (SPH) have gained popularity for the prediction of multi-phase problems [1–3]. Multi-phase SPH models are typically used when two fluids with a large density ratio interact, such as air entrapments in water, droplets in a gas flow, phase change and various other dynamically demanding multi-phase problems [4–8]. In this context, a SPH model was developed by the authors to conduct large-scale multi-phase atomization simulations [9–14]. State-of-the-art multi-phase simulations of air-assisted atomizers require up to billions of particles. This is due to the fact that the dimensions of the injector geometry are in the order of several centimeters, whereas the smallest liquid fragments are in the order of micrometers [15]. Up to now, this spatial range had been resolved with a uniform particle size. Spray characteristics are usually extracted in the close vicinity of the atomizing edge, where the liquid film is fragmented into smaller droplets. A multi-resolution SPH scheme, which allows for the finest spatial resolution close to the atomizing edge and a coarse resolution elsewhere is favorable in such cases. Such a scheme must also be capable of simultaneously handling two immiscible phases, accurately resolving the phase interface and maintaining numerical stability in the presence of high density ratios.

* Corresponding author .
E-mail address: niklas.buerkle@kit.edu (N. Bürkle).

https://doi.org/10.1016/j.cma.2025.118505
Received 4 July 2025; Received in revised form 16 October 2025; Accepted 17 October 2025
Available online 19 November 2025

Research regarding particle refinement in SPH has been conducted for many years. However, the application of multi-resolution SPH schemes to technical flows is still considered as one of the Grand Challenges (GC3) by the SPH community [16]. In the context of astrophysics, the variable-h method was proposed by Hernquist and Katz [17] to address the compressibility in the formation of stars and galaxies and allowing to automatically adjust the particle resolution in regions of higher density. For weakly compressible or incompressible flow physics, splitting and merging particles as a means to increase and decrease particle resolution emerged [18], adding the well known set of disadvantages caused by the erroneous kernel estimates at the resolution interface. Many approaches have been proposed to reduce these errors [19–22].

To address the limitations of splitting and merging approaches while maintaining the flexibility to choose different resolution ratios and preserve flow features like arbitrary-shaped phase interfaces, a natural approach is to handle different resolution levels by separate subdomains. Mass and momentum exchange between these subdomains would then have to be conducted by assessing the fluxes into or out of these subdomains. Many popular approaches have been proposed in this regard, introducing overlapping subdomains and transitioning between different refinement levels by means of interpolation [23,24]. These methods aim to circumvent the Adaptivity Grand Challenge by adding interior boundaries into the computational domain and essentially coupling multiple otherwise independent domains. Unfortunately, boundary conditions (GC2) as well as the coupling to other solvers (GC4) are also considered as Grand Challenges and are not easily accessible. Recently, this kind of overlapping procedure has been gaining popularity, with [25] predicting the von Kármán vortex street resulting from fixed and moving cylinders for various Reynolds numbers involving multiple layers of increasing resolutions in 2D and 3D [26]. The aforementioned works have demonstrated the potential of overlapping methods for single-phase and free-surface flows.

Beyond single-phase formulations, first efforts have been made to extend multi-resolution approaches to multi-phase problems. Initially developed by Chiron et al. [24] for single-phase flows, the Adaptive Particle Refinement (APR) was later extended by Sun et al. [27] to encompass multi-phase flows. In order to achieve this, it was necessary to alter the fluid type of particles which lost their connection to other particles of the same fluid type but different resolution. Doing so, reliable interpolation based on particles of the same phase was ensured. In the resulting multi-phase flow generated by the extended APR scheme, the phase interface appears to be preserved. And while this can be considered as a last resort to avoid crashing of the simulation, it should not be the main reconstruction algorithm, since it can result in a severe transfer of mass from one phase into another, especially for delicate shapes of the interface. However, using this method, Sun et al. [27] were able to successfully predict macroscale phenomena such as a multi-phase dambreak. While this approach works on the macroscale, it should be noted, that locally conserving mass, especially in the vicinity of a phase interface is of utmost importance when considering sensitive liquid fragments such as droplets. In order to be employed in a liquid atomization context, approaches involving overlapping subdomains need further research in order to ensure the preservation of the phase interface. At approximately the same time, Yang and Kong [28] developed another adaptive spatial resolution method for multi-phase SPH. Their approach involves concepts of the variable-h method, refining particles in a confined distance to the phase interface. It was demonstrated in scenarios incorporating two fluids of different phases, such as a dambreak and a drop impact. Recently, Cheng et al. [29] utilized the APR method to simulate viscous rising bubbles, also confining the resolution limit in a fixed distance to the interface. Their findings demonstrated good agreement with uniform predictions. The mentioned methods by Yang and Kong [28] as well as Cheng et al. [29] have their own advantages and drawbacks and would indeed be suitable for adaptively refining the phase interface. However, their main use is when refinement is applied in a constant distance to the phase interface, and hence, when the refinement levels move with the evolving phase interface. Typically, the phase interface where a density ratio of up to one order of magnitude is present is often the cause of problems in numerical schemes. Of course, it is very advantageous if a method is able to avoid this problem at a constant distance. The mentioned methods generally omit the ability to transport this interface across resolution limits. However, the spray in fuel atomization can be very dense. It consists of thousands of liquid fragments of various sizes, extending over the whole domain. In this scenario, adaptive particle refinement can lead to an extensive refinement of the whole computational domain up to the outlet (cf. Fig. 1). In that case, a static refinement with interface reconstruction is likely beneficial and able to confine the zones with higher resolution to just the area of interest while also preserving the interface at the resolution limit. This is a feature, which an adaptive particle refinement in a confined distance to the interface is not meant to. Ideally, of course, a combination of the two refinement strategies would be employed. However, to the authors knowledge, presently no static refinement approach exists which has these capabilities in order to be used for the simulation of liquid atomization.

In this work we present a multi-resolution framework suitable for multi-phase flows, incorporating many of the above discussed features. The multi-phase SPH scheme is presented in Section 2. The multi-resolution method introduced in this work comprises an overlapping technique, which was designed for multi-phase flows. This method will be introduced in Section 3. In Section 4, the functionality is demonstrated by considering a cavity flow, Taylor–Green flow, a Kelvin–Helmholtz instability and an oscillating droplet moving through the resolutional transition zone. A highlight will be a demonstration of a planar atomization case at the end of this section. Finally, in Section 5, important findings are summarized.

2. Methodology

In Section 2.1, the set of equations used to model multi-phase flows is presented. The transport equations are valid far away from the resolution transition zone. SPH particles for which these transport equations are solved will be called regular particles. Later in Section 2.2, the particle redistribution scheme as applied in this work will be discussed.

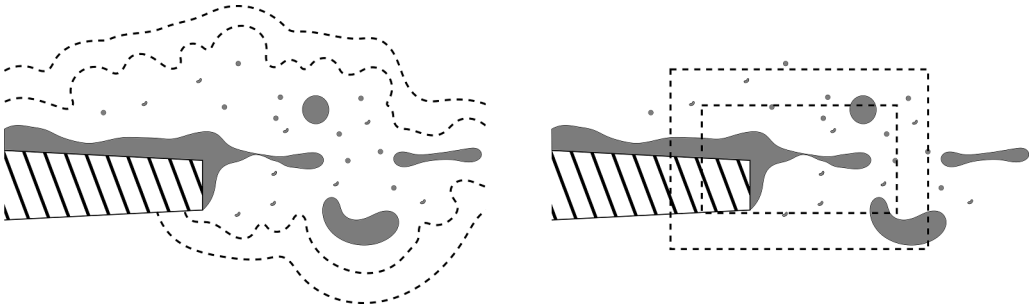

Fig. 1. Different refinement strategies for shear-flow driven liquid atomization. Left: Moving resolution limit in confined distance to the phase interface. Right: Static refinement with interface reconstruction. The generic atomizer geometry is based on the work of Braun et al. [10].

2.1. Governing equations

The density ρ is obtained by a variant of the continuity equation [30]. Following the δ-SPH model of Antuono et al. [31], a diffusion term is added:

$$\left\langle \frac{\mathrm{d}\rho}{\mathrm{d}t} \right\rangle_i = \rho_i \sum_j (\mathbf{u}_i - \mathbf{u}_j) \cdot \nabla W_{ij} V_j + \delta\, c_\chi \sum_{j \in \chi} (\rho_i - \rho_j) \left(\frac{\mathbf{r}_{ij}}{\|\mathbf{r}_{ij}\|} \cdot \nabla W_{ij} \right) V_j, \tag{1}$$

with $\mathbf{u}$ denoting the velocity, $\mathbf{r}_{ij} = \mathbf{r}_i - \mathbf{r}_j$ the distance vector, ∇W_{ij} the kernel gradient between particles i and j, V the particle volume and c_χ the speed of sound of fluid type χ. The δ-SPH model was originally proposed by Antuono et al. [31] to reduce density fluctuations caused by the 0th order approximations in SPH. Throughout this study the scaling factor δ is set to 0.1. If not mentioned otherwise, the particle sums $\sum_j$ are always conducted using the particles j of the same resolution. However, the density is only diffused between particles of the same fluid type χ, in order to avoid the unphysical flux across the density jump of the phase interface.

A formulation of the momentum equation is chosen, which is capable to handle interfacial flows with high density ratios [32]:

$$\left\langle \frac{\mathrm{d}\mathbf{u}}{\mathrm{d}t} \right\rangle_i = -\sum_j \frac{p_j \pm p_i}{\rho_j \rho_i} \nabla W_{ij} m_j + \mathbf{a}_{visc,i} + \mathbf{a}_{surf,i}, \tag{2}$$

with the pressure p, particle mass m and the accelerations originating from the viscosity term $\mathbf{a}_{visc}$ and the surface tension term $\mathbf{a}_{surf}$. The viscosity $\mathbf{a}_{visc}$ and surface tension $\mathbf{a}_{surf}$ terms are modeled according to the works of Szewc [33] and Adami et al. [34], respectively. *Tensile instability control* (TIC) is performed by means of the pressure gradient formulation [35]. It should be noted that when using the minus-form of the pressure gradient, TIC does not conserve linear and angular momentum for truncated kernel supports. In free-surface flows, a detection algorithm must therefore be employed to prevent such unphysical behavior. We employ a weakly-compressible equation of state, the barotropic Tait equation [36]:

$$p_i = \frac{\rho_{0,\chi} c_\chi^2}{\gamma_\chi} \left[\left(\frac{\rho_i}{\rho_{0,\chi}} \right)^{\gamma_\chi} - 1 \right], \tag{3}$$

with the reference density ρ_0.

The time integration is conducted by a modified Velocity-Verlet scheme [37]. In this work we utilize the pairing-stable Wendland C4 kernel, allowing for a larger number of neighbors [38], unless specified otherwise. The default ratio of h/dx is set to 2.0. This kernel choice is motivated by the need to accurately resolve vortex dynamics in atomization [14,39,40] and is likewise widely adopted in domain-decomposition approaches [24,25]. The compressibility of the fluids will be modeled with $\gamma = 1$ and $\gamma = 7$ for gases and liquids, respectively, following previous studies of interfacial flows [32]. For $\gamma = 1$, the equation of state simplifies to the popular linearized equation of state [27,35,41,42], physically representing an isothermal ideal gas.

2.2. Particle redistribution

It is well known that convergence, consistency and stability (GC1) in SPH are strongly affected by the regularity of the particle distribution [16]. Especially in vicinity of an internal boundary as it is common with multi-resolution approaches, the spatial particle distribution may be strongly irregular. This is expected to undermine the consistency of the interpolation used for domain coupling [24,25]. In earlier SPH codes, redistribution is conducted by simply adding a background pressure [43], a strategy which is judged as critical today, since it may cause excessive numerical dissipation [44] and dispersion [43]. This is due to the artificial pressure gradient based on particle anisotropy, which induces unphysical velocity fluctuations which in turn mitigate the original anisotropy. By contrast, a particle regularization scheme that reorders particles after the momentum equation has been solved [45] can reorder particles without introducing extra numerical fluctuations. Many so-called shifting methods have been developed to counteract irregular particle distributions [45–47]. However, applying these schemes, the spatial particle distribution is regularized, but the resulting additional displacements are not accounted for in the mass and momentum equations. Neglecting these contributions to the mass and momentum equations and simply using shifting schemes as a means of restoring particle order is still a popular choice nowadays,

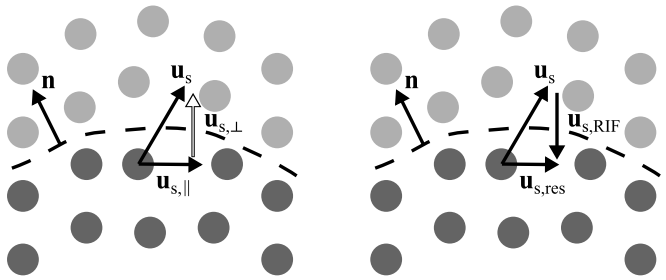

Fig. 2. Correction of shifting vectors at the phase interface due to similar approaches. Left: Decomposition into components. Right: Repulsive interface force.

even for multi-resolution approaches [24]. In contrast to regular shifting approaches, in ALE and transport-velocity schemes the fluxes induced by the displacement of the particles can be accounted for [44,48].

For the following considerations, we adopt the approach of Adami et al. [44] as a starting point, since its transport-velocity formulations involve only a minimal set of flux terms. This simplification is justified when the advection velocity is significantly larger than the shifting velocity [48]. Moreover, in well-resolved simulations the amount of shifting is naturally reduced, which in turn diminishes the relevance of shifting-induced fluxes [27,41]. A potential drawback of neglecting these fluxes is the occurrence of volume drift in confined domains [27]. We emphasize, however, that in cases where such drift becomes substantial, incorporating the fluxes would indeed be advisable. Furthermore, it has been shown that incorporating these fluxes can improve the scheme's performance in turbulent flows [49], although some of the inherent limitations of traditional SPH remain [50]. Still, the inclusion of these fluxes is not a fundamental requirement of the proposed multi-resolution framework herein.

Following Adami et al. [44], the transport-velocity $\mathbf{u}_t$ is decomposed into the fluid-velocity $\mathbf{u}$ as obtained by the momentum equation and the shift-velocity $\mathbf{u}_s$. In the context of transport-velocity and ALE schemes, the fluid-velocity $\mathbf{u}$ is also commonly referred to as the Lagrangian velocity. The transport-velocity is then used for updating the particle position $\mathbf{x}$:

$$\mathbf{u}_t = \mathbf{u} + \mathbf{u}_s, \qquad \mathbf{x}^{n+1} = \mathbf{x}^n + \int_n^{n+1} \mathbf{u}_t \, \mathrm{d}\tau. \tag{4}$$

It should be noted here, that this decomposition enables in the limiting case the Eulerian treatment of the particles, as the fluid-velocity can be completely counteracted by the shift-velocity. However, for SPH simulations with moving phase interfaces, a Lagrangian particle motion is preferred. Therefore, the shift-velocity has to be significantly smaller than the actual fluid-velocity $\|\mathbf{u}_s\| \ll \|\mathbf{u}\|$. Furthermore, phase interfaces need to be well-resolved. Hence, from the empirical knowledge summarized above, we neglect these ALE fluxes and assume the shifting displacements far away from the resolutional transition zone to be very small. In this context, the scheme simply enables the access to the unadulterated fluid-velocity or Lagrangian velocity $\mathbf{u}$, while still redistributing the particles. The unadulterated fluid-velocity is the part of the velocity field, which is not affected by the small scale noise that would otherwise result from a particle redistribution scheme such as the background pressure. Furthermore, an accurate representation of the fluid velocity must be used for the interpolation of the flow fields between coupled subdomains, since the shifting velocity can be in the order of the fluid velocity in vicinity of an internal boundary. On top of this, shift velocities of two adjacent subdomains are generally uncorrelated.

For the shifting scheme, it is necessary to distinguish between SPH particles which are located far away from any phase interface and internal boundary, and those that are not. For the former particles, the regular shifting scheme proposed by Lind et al. [45] is applied:

$$\mathbf{u}_{s,i} = -\xi_{\mathrm{Shift}} \left(\frac{h}{\delta t}\right)^2 \sum_j V_j (1 + f_{ij}) \nabla W_{ij} \, \delta t, \tag{5}$$

$$f_{ij} = \xi_{\mathrm{Rep}} \left(\frac{W_{ij}}{W(dx)}\right)^n. \tag{6}$$

with the time step width δt and tuning parameters ξ_{Shift}, ξ_{Rep} and n. The term f_{ij} introduces additional repulsive shift velocities. Hence, particles are more evenly distributed. Typical choices for these parameters are $\xi_{\mathrm{Shift}} = 0.5$, $\xi_{\mathrm{Rep}} = 0.1$ and $n = 2$. This scheme was originally designed for single-phase and free-surface flows. For multi-phase flows, the treatment of the interface has to be tuned. The goal is to minimize particles being stripped off from the interface, in order to prevent the interface to become interrupted and noisy. It is common practice to apply some kind of interface detection to identify particles in contact with the free-surface. Free-surface detection algorithms are available in the literature, ranging from simple to more advanced approaches [45,51]. Typically the shifting of these particles in the direction normal to the interface is suppressed by removing the corresponding normal component [45,52]. In this work, however, we eliminate the component in normal direction by counter-balancing it with a repulsive interface force (RIF). As illustrated in Fig. 2, both approaches are similar concerning the outcome. In Fig. 2 (Left), only the parallel shift vector $\mathbf{u}_{s,\parallel}$ is accounted for. A similar resulting shifting velocity $\mathbf{u}_{s,res}$ can be obtained by counter-balancing the normal component by $\mathbf{u}_{s,RIF}$ (cf. Fig. 2 Right). In case of free-surface flows, only the correction by decomposition is possible.

As stated previously, this work is focussed on multi-phase flows not on free-surface flows. The goal is to avoid mixing of particles of different fluids. In order to avoid the potentially costly free-surface detection, we simply add a *Grenier*-style repulsive interface force (RIF) [53]:

$$\mathbf{u}_{s,i} = -\underbrace{\xi_{\text{Shift}}\left(\frac{h}{\delta t}\right)^2}_{\substack{\text{Kinematic}\\ \text{pseudo-pressure}}}\left(\underbrace{\sum_j V_j(1+f_{ij})\nabla W_{ij}}_{\text{Regular}} + \underbrace{\xi_{\text{RIF}}\alpha_i \sum_{j\notin\chi} V_j \nabla W_{ij}}_{\text{RIF}}\right)\delta t. \tag{7}$$

Both, the regular shifting as well as the RIF scale with the same kinematic pseudo-pressure. However, the RIF accounts only for particles of a different fluid χ. Hence it separates the fluids at the phase interface strictly within a mean particle distance. As will be shown in Section 3.4.1, this RIF also facilitates smooth blending with one of the interface reconstruction algorithms applied at the resolution boundary. It should be emphasized that the purpose of the RIF is simply to counteract the non-physical, small-scale deformation of the interface caused by particle shifting. Consequently, a limit $\xi_{\text{RIF}} \ll 1$ is necessary. Preliminary tests yielded $\xi_{\text{RIF}} = 0.05$ as maximum value. Hence, we restrict ξ_{RIF} to 0.01. Doing so, the movement of the phase interface is still anticipated to be dictated by the momentum equation.

3. Multi-resolution approach

The present approach includes many state-of-the-art techniques used by the SPH community. Some of which never have been used before in the context of particle refinement. Our framework represents a synthesis of both established methods and novel approaches. The most important features of our multi-resolution approach for multi-phase flows are as follows:

- Transport-velocity approach
- Multi-resolution coupling via domain decomposition
- Continuous particle generation and deletion
- Reconstruction of the phase interface

Except for the first item, these operations are exclusively carried out at the internal boundary. The last one is only necessary for multi-phase flows. The transport-velocity approach was already introduced in Section 2.2. Its necessity is manifested by the need of the unadulterated fluid-velocity for interpolation of the flow state between the subdomains at different spatial resolution. The remaining features will be discussed below.

3.1. Aspects of novelty

The novelty of this work lies in the extension of popular domain decomposition approaches used for multi-resolution SPH to multi-phase flows with focus on surface tension driven phenomena. Both, the employed continuous particle generation and deletion as well as the reconstruction of the phase interface have previously not been applied in multi-resolution SPH. The new framework should enable us to conduct simulations where the interface moves freely and undisturbed between resolution levels, as opposed to other approaches where the refinement is conducted in a safe distance to the phase interface.

3.2. Multi-resolution coupling via domain decomposition

In our framework, we follow the terminologies of Bian et al. [23] and Chiron et al. [24]. Similar to the approach of Chiron et al. [24], mediating particles are employed, the so-called guard particles. These initially inactive particles are used to conduct certain operations on them until they are eventually switched to active particles. It is a popular concept, newly created guard particles are kept inactive until their position allows them to be switched to active particles or in this framework: to regular particles (cf. Fig. 3). Doing so, ideal conditions can be ensured before the particles are activated. Until then, their flow state is determined by the other resolution via interpolation. A popular choice is to spatially redistribute the guard particles, and hence, ensure an optimal particle distribution the instant that they are converted to active particles. This strategy increases the quality of the predictions of such multi-resolutional approaches. The guard particle concept is applicable independent of how the particles are created and deleted at the internal boundary. Chiron et al. [24] applied splitting, whereas Bian et al. [23] used a boundary condition approach similar to the one presented in this work.

The main principle of the applied multi-resolution coupling is based on the works of Bian et al. [23] and Chiron et al. [24]. Our framework extends these approaches to multi-phase flows. Refinement levels are treated as separate bounded subdomains (cf. Fig. 4). The transition of the flow states between subdomains at different refinement levels is performed by interpolation. The refinement ratio used in this work is $m_{\text{i,coarse}}/m_{\text{i,fine}} = 4$, if not mentioned otherwise. For the interpolation between the different resolution levels,

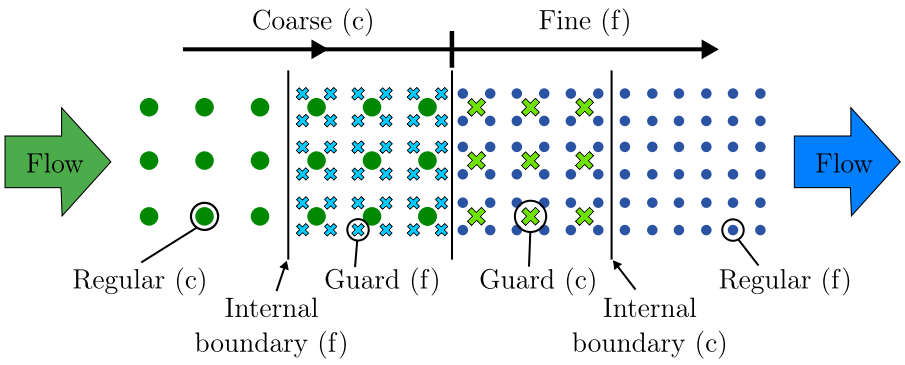

Fig. 3. Resolution transition by means of guard particles. Adapted from Chiron et al. [24].

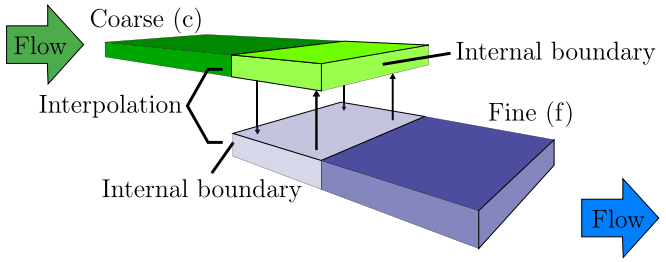

Fig. 4. Two separate subdomains, partly occupying the same space, coupled via interpolation.

the Shepard-Interpolation [54] of quantity ϕ is used[1]:

$$\langle \phi \rangle_i = \frac{\sum_{j \in \Omega} V_j \phi_j W_{ij}}{\sum_{k \in \Omega} V_k W_{ik}}, \tag{8}$$

with Ω the set of particles of the domain at different resolution and same phase as particle i.

We subdivide the mediating particle class into not only guards, but additionally boundary particles and constraints. Boundary particles are guard particles in contact with the internal boundary and are either gaining or losing mass, depending on the flow direction. Constraint particles are an intermediate particle between guard and regular particle, as introduced by Bian et al. [23]. The constraints allow for blending between the guards and regular particles. As consequence, more aggressive operations can be conducted on the guard particles. These operations are then attenuated and applied to constraint particles and finally smoothly blended into the operations conducted on regular particles.

The detailed operating principle is depicted in Fig. 5. In order to improve the visibility, the two subdomains are shifted apart in vertical direction. In the real configuration, particles of different resolution co-exist at the same location, but only influence each other indirectly through interpolation. A fluid mass element, transitioning between domains of different resolutions is initially part of particle A. Once it is transferred from one resolution level to the other, it is represented by particle B. During this procedure the coarse particle A will traverse the following spatial regions:

1. Interpolation region, where the particle A serves as a data point for interpolation onto the guard and constraint zone of the corresponding other resolution.
2. Overlap region, where it is still treated as a regular particle
3. Constraint zone, an intermediate step between regular zone and guard zone. The flow state of particle A is partly determined by the transport equations like a regular particle, and partly determined by the fine resolution like a guard particle. A constraint particle is subject to interface reconstruction in case of multi-phase flows.
4. Guard zone, where the particle flow state is determined solely by the corresponding other resolution. In addition, the guard zone is bounded by static ghost particles, to avoid guards being shifted out of the domain. Guard particles are also subject to interface reconstruction.

[1] It should be noted that, since transport-velocity approaches are advantageous in turbulent flows, applying the multi-resolution framework in this context may seem natural. However, initial tests showed that Shepard-Interpolation may not adequately capture small-scale turbulent fluctuations on the order of the kernel support. Significantly increasing the resolution is one option, while moving-least-squares (MLS) interpolation also appeared to improve interpolation accuracy, consistent with Ricci et al. [25].

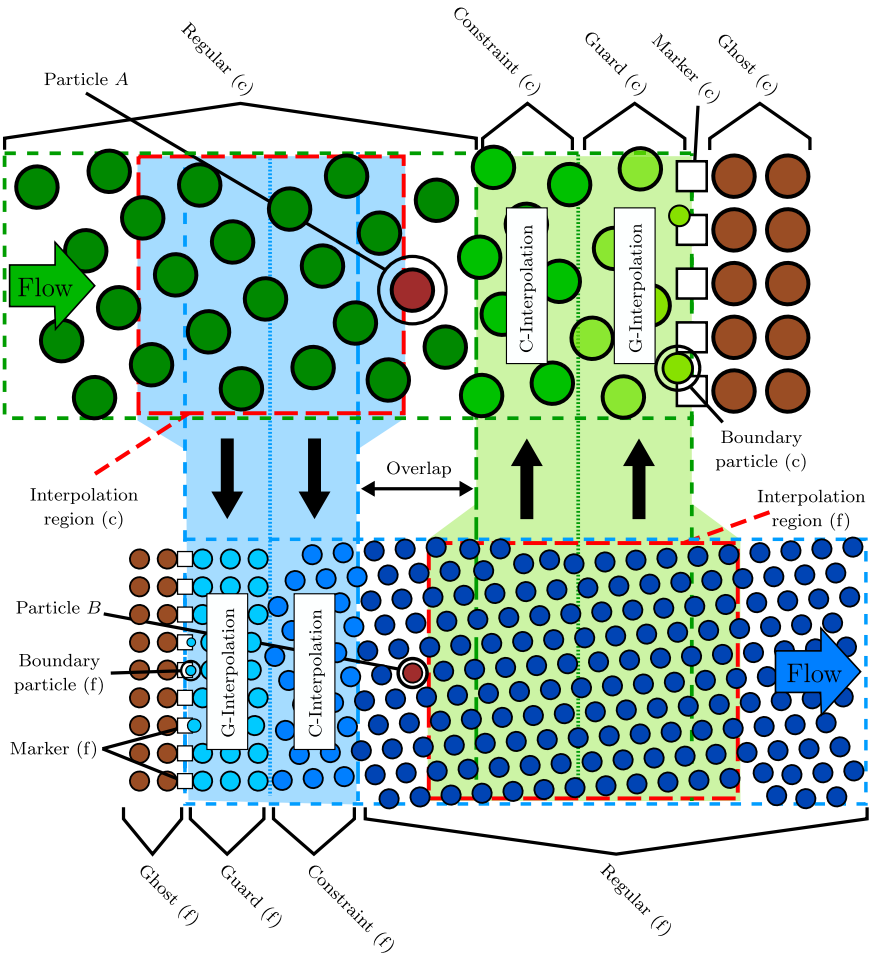

Fig. 5. Principles of the flow state interpolation at the internal boundary.

5. Boundary layer, where the particle A is in contact with the boundary comprised of markers. A particle in this layer switches its type to boundary particle for further identification. In case of outflow, particle *A* will be deleted. A more detailed explanation of this process will be given in Section 3.3.

If particle *A* is moving through these regions, it will be changing its type from regular to constraint and subsequently to guard and boundary particle before it is finally deleted. The boundary particle is a sub-class of guard particles, with the distinction that the mass of the boundary particle increases or decreases at the internal boundary.

As soon as particle *A* enters the interpolation region and exhibits an velocity directed outside of its subdomain, in the illustration to the right (cf. Fig. 5), an increase of the mass is imposed in the corresponding other subdomain. There, the newly created boundary particle *B* will pass through the same regions, but in reversed order. Finally, particle *B* is now the only particle representing the fluid mass inside of the fine resolution level. The operations conducted inside of these different regions and a more detailed discussion of the particle treatment will be presented in the following subsections.

3.2.1. Interpolation region

Particles inside the interpolation region serve as data points for the flow state interpolation of the corresponding other resolution level. The interpolation region is completely filled with regular particles. An outward flow inside the interpolation region directed towards the internal boundary of one subdomain is causing a mass increase on the other resolution level. The interpolation is conducted for the markers, boundary particles, guards and constraint particles. In this study, Shepard-Interpolation [54] is used in this regard. In addition, to avoid constraint particles being present inside the kernel support during interpolation the overlap region is required.

3.2.2. Overlap region

Particles inside the overlap region are regular particles. Solutions from both resolution levels coexist in this region. This region ensures that particles from the adjacent constraint zone are not used as data points for interpolation. Bian et al. [23] observed an

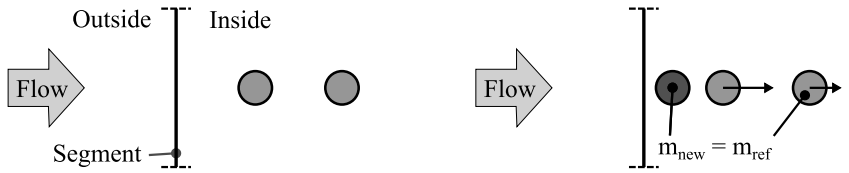

Fig. 6. Sudden mass increase and perturbation of the already existing particles in vicinity to a boundary segment during inflow. Particle distribution before (left) and after (right) insertion.

increase in accuracy with greater overlap. Using an overlap of at least the size of the kernel radius, ensures the kernel support to be filled only with regular particles during interpolation.

3.2.3. Constraint zone

Particles in this zone receive an initial constraint in terms of interpolated velocities and pressures by means of Shepard-Interpolation at the beginning of the time step. Subsequently, during the course of a time integration step, the density and momentum of the constraint particles are adjusted in the same way like regular particles according to Eqs. (1)–(3).

Consequently, for constraint particles, the time integration of the quantity ϕ during the predictor and corrector step follows the equations:

$$\phi_i^{n+1/2} = \phi_i^{n,constr} + \left\langle \frac{\mathrm{d}\phi}{\mathrm{d}t} \right\rangle_i^n \frac{\delta t}{2}, \tag{9}$$

$$\phi_i^{n+1} = \phi_i^{n,constr} + \left\langle \frac{\mathrm{d}\phi}{\mathrm{d}t} \right\rangle_i^{n+1/2} \delta t, \tag{10}$$

where the first term on the RHS $\phi_i^{n,constr}$ is the constraint obtained from the interpolation over the corresponding other resolution (cf. Eq. (8)). In case of $\phi = \mathbf{u}$, the accelerations $\mathbf{a} = \langle \mathrm{d}\phi/\mathrm{d}t \rangle$ are obtained by the momentum equation. Additionally, the pressure is interpolated and the density $\rho_i^{n,constr}$ is then estimated according to Eq. (3). Subsequently, the density update follows the same pattern. The positions of the constraint particles are subject to regular shifting and interface reconstruction.

3.2.4. Guard zone

Guard particles obtain their flow state solely by interpolation. Both, the velocity and the pressure are interpolated using the regular particles inside of the interpolation region of the corresponding other resolution. The density is then estimated according to Eq. (3). The positions of the guard particles are subject to regular shifting and interface reconstruction.

3.2.5. Boundary zone

Unlike the regions discussed before, this region is rather a layer of particles which are in contact with the segments of the internal boundary. Affected are particles whose volumes protrude over the subdomain boundary. A guard that moves towards its internal boundary and subsequently sticks to one segment of that boundary will switch its type to boundary particle, to further ease its identification in the following mass deletion. Likewise, a growing boundary particle that has reached the reference mass is released as a guard particle and no longer sticks to the boundary. A continuous generation and deletion of particle mass is performed at the internal boundary by an algorithm proposed by Werdelmann et al. [55]. The boundary segments are represented by markers, a special particle type that does not directly interact with any other particle. Instead, a marker evaluates the flow state at its associated boundary segment. The operating principle will be explained in detail in Section 3.3.

3.3. Continuous particle generation and deletion

To avoid pertubations of the flow as they occur when the mass in a subdomain is suddenly increased or decreased by a whole particles reference mass (cf. Fig. 6), a smooth incrementation of the mass must be conducted. This is a well-known challenge when treating boundary conditions in SPH [56]. The quality of the imposed flow states in vicinity of the internal boundary strongly depend on the local particle disorder. Hence, the particle regularization (Section 2.2) and particle mass incrementation algorithm in this section are strongly connected and care must be taken in the implementation of the mass incrementation.

To avoid a sudden increase or decrease of mass in one subdomain, we pursue an approach, in which particles are continuously growing and shrinking. We assume that the mass m_p^n of particle p at time instant n is the manifestation of the part of its spatial extent that protrudes into a subdomain (cf. Fig. 7). The further ingress or egress of the particle into the area is realized by an increase or decrease of the particle mass. The shrinking or growing boundary particle is sticking to the boundary segment until it is deleted or has reached the reference mass $m_{ref} = \rho_0 V_0$, depending on the flow direction. When it reaches the reference mass, the particle is released.

In this work, a continuous mass insertion and deletion algorithm as originally proposed by Werdelmann et al. [55] is applied to the particles extending into or out of the computational domain. In the original publication many special cases are discussed. In the following, we will only explain the basic operating principle. A subdomain is bounded by a series of segments. On these segments

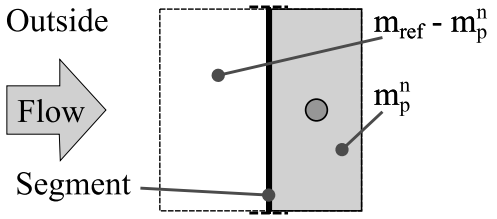

Fig. 7. A particle is protruding into a subdomain.

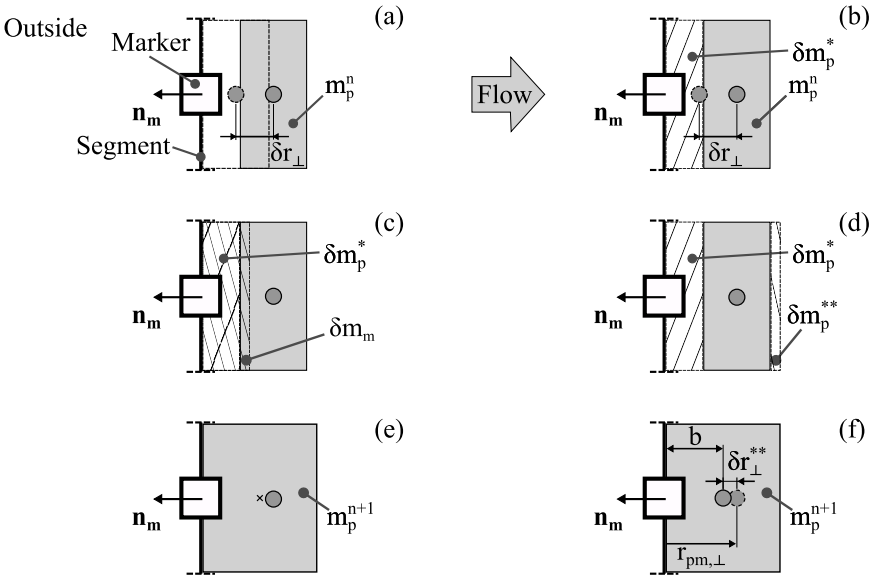

Fig. 8. Mass incrementation algorithm at a single boundary segment under inflow conditions. (a) Position of the boundary particle after time integration. (b) Compute intermediate particle mass increment. (c) Compute marker mass increment. (d) Distribute marker mass imbalance. (e) Apply mass increments. (f) Correct particle position.

markers are placed. A marker is a special type of particle that does not directly interact with the particles. The state of the marker is also updated by Shepard-Interpolation. The operating principle of the algorithm for particle generation and deletion is illustrated in Fig. 8. The mass incrementation of the mass of particle p from m_p^n to m_p^{n+1} is depicted. The boundary segment is represented by a line, with the corresponding marker located at the center. The face normal of that segment is pointing towards the outside of the domain. A particle is shown that moves further into the subdomain and subsequently its mass is increasing. To aid visualization, we assume constant density. This allows for the mass and its increase to be represented by volumes, and more specifically areas in 2D. The center of the particle is depicted by a circle, its spatial extent is represented by the gray shaded rectangular area. This spatial extent is equal to its mass. Mass increments δm, which are added on top of the particle mass at the end of the process are indicated as hatched areas.

The mass variation associated with a mass flux into or out of the domain is achieved by the following steps. The enumeration points correspond to that of Fig. 8(a)–(f):

(a) After the positional updates of the boundary particles, they are no longer in contact with their corresponding boundary segment.
(b) Compute an intermediate mass increment for existing boundary particles. This mass increment is based on the movement relative to the boundary $\delta r_\perp$.
(c) Compute mass increments at the marker positions based on it's density and fluid velocity. This increment is partly covered by the intermediate increment. Then evaluate the imbalances between these increments.
(d) Distribute the marker mass imbalance to the closest boundary particles. Evaluate residual imbalances and create new particles if no boundary particles are in contact.
(e) Apply the mass increments to the boundary particles. The particle position is no longer coinciding with its barycenter.
(f) Correct particle position in order to center the particle position in the new mass element.

These steps will now be explained in detail. First, after the update of the particles position, the particle is no longer in contact with its corresponding boundary segment, as it is depicted in Fig. 8(a). Hence, the intermediary mass increment is calculated based

on the perpendicular distance of the particles spatial extent to the internal boundary $\delta r_\perp$ (cf. Fig. 8(b)):

$$\delta m_p^* = \underbrace{-\delta \mathbf{r} \cdot \mathbf{n}_m}_{\delta r_\perp} A_{ref}\, \rho_p, \tag{11}$$

with the reference area of the particle $A_{ref} = dx^{dim-1}$. This mass increment δm_p^* is not necessarily identical to the increment that will be calculated at the boundary segment represented by the marker δm_m (cf. Fig. 8(c)). In order to cope with this imbalance, at first, a mass increment to the marker is to be calculated:

$$\delta m_m = -\mathbf{u}_m \cdot \mathbf{n}_m\, A_{ref}\, \rho_m\, \delta t. \tag{12}$$

The velocity $\mathbf{u}_m$ and density ρ_m of the marker is interpolated by means of Eq. (8). In general, multiple particles can be in contact with a single boundary segment, as well as a boundary particle reference area can overlap with multiple boundary segments. Imbalances have to be evaluated for all the segments and particles in contact. In this description, we focus on the simplest case. Additional details can be found in Werdelmann et al. [55]. The imbalance for a single particle reference area in contact with a single boundary segment is calculated by:

$$\delta m_p^{**} = \delta m_m - \delta m_p^*. \tag{13}$$

This mass increment is then distributed over all boundary particles which are in contact with the boundary segment. In the present case it is just the particle p, as illustrated in Fig. 8(d). If after the update, the mass m_{p1}^{n+1} of particle p_1 would exceed the particle reference mass due to the marker imbalance δm_p^{**}, another boundary particle p_2 is created at the marker position with the residual mass increment:

$$m_{p1}^{n+1} = m_{p1}^n + \delta m_{p1}^* + \delta m_{p1}^{**} = m_{ref}, \tag{14}$$

$$m_{p2}^{n+1} = \delta m_{p2}^{**}, \qquad \text{with} \qquad \delta m_{p2}^{**} = \delta m_p^{**} - \delta m_{p1}^{**}. \tag{15}$$

The newly created particle p_2 obtains its velocity and density from the nearest marker. Thereafter, the mass increments are applied and the particle mass is updated. The updated particle mass is then given by

$$m_p^{n+1} = m_p^n + \underbrace{\delta m_p^* + \delta m_p^{**}}_{\delta m_p}. \tag{16}$$

The mass increments δm_p^* and δm_p^{**} are added to the boundary segment. Hence, the mass represented by these increments should extend inwards from the boundary segment and still be in contact with the boundary. Thus, adding the increments to the particle will move its barycenter as indicated by a cross in Fig. 8(e). For the particle barycenter to coincide with its position again, a shift $\delta r_\perp^{**}$ in direction of $\mathbf{n}_m$ (cf. Fig. 8(f)) is necessary. This concluding shift vector is obtained by subtracting the new particles spatial extent b from its normal distance to the marker $r_{pm,\perp}$:

$$\delta \mathbf{r}_\perp^{**} = \mathbf{n}_m \left(\underbrace{\mathbf{r}_{pm} \cdot \mathbf{n}_m}_{r_{pm,\perp}} - \underbrace{\frac{m_p^{n+1}}{2\,\rho_p\, A_{ref}}}_{b} \right). \tag{17}$$

Until the reference mass is reached, the growing particle p is always in contact with the boundary segment. After that, it switches its type to guard. In case of outflow, if the updated particle mass is zero, the particle is deleted. If adding the mass increment δm_p^{**} is not possible due to the particle reaching negative mass, the particle mass is reduced to zero and the particle deleted. The residual mass increment is kept and applied to the next particle during the next timestep.

3.4. Reconstruction of the phase interface at the internal boundary

Creating SPH particles at the phase interface is an erratic process. In order to preserve the phase interface, further measures are required. This necessity is illustrated in Fig. 9. A time instant is shown where a liquid fragment is transitioning from the fine to the coarse domain. At the fine spatial resolution, the interface is predicted (cf. Fig. 9(a), blue line). The coarse particles are generated at the internal boundary. At the coarse resolution, the interface is the result of the erratic particle creation process. Without any additional reconstruction mechanisms, the phase interface of the coarse resolution is distorted and gas inclusions as well as liquid particles in the gaseous phase may be generated (cf. Fig. 9(b)). As surface tension effects strongly depend on the local curvature of the interface, it is essential to preserve the interface when crossing from one to the other resolution level. For the selected overlapping approach, there is always at least one subdomain, in which the location of the phase interface can be derived from first principles (momentum equation). We intend to exploit this behaviour to transfer the shape and position of the phase interface to the subdomain at the different spatial resolution level.

Two mechanisms are used in order to achieve this. The first part consists of a kernel scale reconstruction of the phase interface by redistributing particles with the goal to preserve the real phase interface. This is achieved by adding an inter-resolutional repulsive interface force to the particle redistribution scheme. The goal of the second reconstruction mechanism is to avoid sub-kernel gas

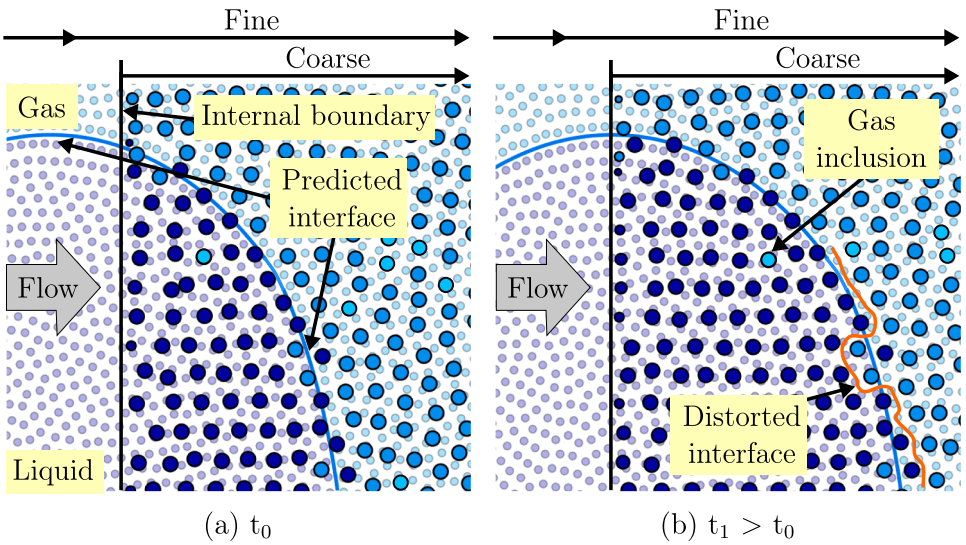

Fig. 9. Comparison of the predicted fine interface and the evolving coarse interface generated without any additional reconstruction mechanisms.

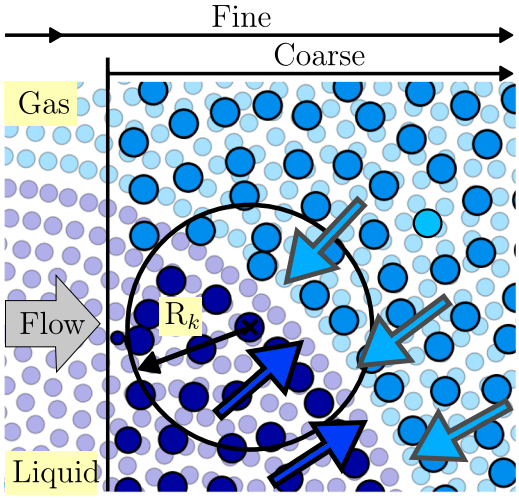

Fig. 10. Inter-resolutional RIF for kernel scale interface reconstruction.

inclusions and liquid particles in the gaseous phase. In order to achieve this, the mass of boundary particles which are not inside their the assigned phase is passed parallel to the internal boundary back into the correct phase. In preparation for this, a mass increment referred to as the color-gradient mass increment (CGMI) is computed. To determine whether particles and boundary segments are covered by their respective phase, a simple kernel sum over particles of the same phase proves sufficient. While more sophisticated interface detection methods could potentially enhance the results, they seem not strictly required in this context.

3.4.1. *Inter-resolutional repulsive interface force*

In Fig. 10 the operating principle of the kernel scale interface reconstruction is illustrated. In the finer resolution domain, the phase interface is derived from the momentum equation. The shape of the interface is then transferred to the coarse resolution by additional terms in the shifting algorithm in Eq. (7). The arrows indicate the direction of these correcting velocities. In order to obtain these, an additional repulsive interface force is imposed acting from the finer gas particles (light blue) on the coarser liquid particles (dark blue) and from the finer liquid particles acting on the coarser gas particles.

The inter-resolutional RIF for interface reconstruction reads:

$$\mathbf{u}_{s,i,IntRec} = -\xi_{\text{Shift}}\ \xi_{\text{IntRec}}\ (1-\alpha_i)\left(\frac{h}{\delta t}\right)^2 \sum_{j\epsilon\Theta} V_j \nabla W_{ij}\ \delta t, \tag{18}$$

with Θ representing the set of particles of different resolution and different fluid type as i. For ξ_{IntRec}, a similar argument applies as for ξ_{RIF} in Eq. (7). Hence, ξ_{IntRec} is set to 0.02. α_i is a scalar used to define on which particles this operation is conducted. As the

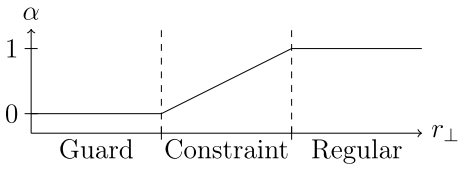

Fig. 11. Blending function α across the perpendicular distance to the internal boundary $r_\perp$.

interface reconstruction is conducted only for guards and constraints, α_i is 1 for every other particle type. For constraint particles, α_i is used as a linear blending function to ensure a gradual transition from interface reconstruction to regular interface prediction via surface tension forces (cf. Eq. (2)) along the distance to the internal boundary. This linear blending function is illustrated in Fig. 11.

The particle shifting scheme (cf. Eq. (7)) with all contributions can then be updated to:

$$\mathbf{u}_{s,i} = \underbrace{\frac{\delta r_i^{**}}{\delta t}}_{\substack{\text{mass}\\ \text{incremen–}\\ \text{tation}}} - \xi_{\text{Shift}} \left(\frac{h}{\delta t}\right)^2 \Bigg(\underbrace{\sum_j V_j (1 + f_{ij}) \nabla W_{ij}}_{\text{Regular}} + \underbrace{\xi_{\text{RIF}}\, \alpha_i \sum_{j \notin \chi} V_j \nabla W_{ij}}_{\text{RIF}} + \underbrace{\xi_{\text{IntRec}}\, (1 - \alpha_i) \sum_{j \in \Theta} V_j \nabla W_{ij}}_{\text{Interface reconstruction}} \Bigg) \delta t. \tag{19}$$

It should be noted here, that these artificial shifting velocities do not impact the Lagrangian velocity. The overall momentum is not directly affected.

3.4.2. Color-gradient mass increment

In the following, we will address how phase encapsulations develop and how to avoid it. The kernel support R_k which serves for the interpolation of particle and marker velocities is used for the evaluation of fluxes at the internal boundary. It covers multiple particle distances. The phase interface, however, is a sub-kernel scale discontinuity. Hence, applying only kernel scale reconstruction mechanisms will not be sufficient to preserve the phase interface. Furthermore, releasing boundary particles which did not reach their final volume is not advisable as very different particle volumes may cause instabilities of the particle distribution. To avoid this, particle masses and volumes should be as close as possible to the reference value. For this reason, instead of releasing a particle prematurely, its mass is shifted away from the opposite fluid.

Consider the gaseous boundary particles p_1 and p_2 which are located in vicinity to the phase interface, as depicted in Fig. 12(a). These particles are generated at their assigned gaseous markers m_1 and m_2. To facilitate the illustration, only the gaseous markers and boundary particles are shown which could subsequently cause gas inclusions. The particles of the fine spatial resolution are not visible. Only the predicted phase interface is shown. Due to the gaseous inflow before the time instance t_0, particle p_1 is close to the reference mass. As illustrated in Fig. 12(a), at the time instance t_0, the gaseous marker m_1 is isolated, as it is partly covered by the predicted liquid phase and does not increase or decrease gaseous mass at its position. At this point, if the mass of p_1 is between $0.95\,\mathrm{m}_{ref} \leq \mathrm{m}_{p1} \leq \mathrm{m}_{ref}$ and the marker m_1 is covered by the other phase, p_1 is prematurely released as a guard particle. In some cases however, the mass of particle p_1 will be significantly lower than reference mass meaning that it cannot be released. Furthermore, the mass of p_1 may continue to increase after the particle is encapsulated by the liquid, since it is in contact with the marker m_2 as well (cf. Fig. 12(b)). Unlike m_1, m_2 is not yet separated from the gaseous phase and only partly covered by liquid. Up to the moment when the marker m_2 is covered by liquid, it will continue to distribute mass to particle p_1 according to the contact area $\mathrm{A}_{\text{contact},m2,p1}$. In that case, particle p_1 must not be released in order to avoid encapsulations and distortions of the interface. Particle p_1 may even continue to accumulate mass beyond the reference mass. However, not releasing the particle and keeping it at the internal boundary until the liquid fragment has passed is violating the local mass conservation. For this reason, a mass increment will be computed for p_1. This mass increment is then moved parallel to the boundary and distributed to the particle p_2 where it can be manifested in a gaseous particle that subsequently may be released as a guard particle and not cause any encapsulations.

It should be noted, that the inter-resolutional RIF would be sufficient to address phase encapsulations (cf. Fig. 12(b), orange trajectory), provided that the overlap of the subdomains is sufficiently wide and these encapsulations are at most one kernel radius away from the interface. However, to minimize guard and constraint zone sizes in order to reduce the computational overhead, an additional correction mechanism has to be applied. The approach is to determine a mass increment on basis of the gradient of a color function (cf. Fig. 12(b) green normalized vector $\hat{\mathbf{n}}_c$), the color-gradient mass increment (CGMI). This increment serves to transfer mass parallel to the boundary (vector $\mathbf{p}$) into the correct phase. Hence, mass is taken from particle p_1 by marker m_1 and subsequently passed to m_2 which distributes the mass to particle p_2. From particle p_2 onwards, it may be passed further up, depending on the local gradient of the color function. This procedure is explained in the following.

The gradient of the color function is calculated at the marker position m:

$$\nabla c_m = \sum_{j \in \Theta} \nabla W_{mj} V_j \tag{20}$$

similar to the computation of the inter-resolutional RIF, this calculation is conducted using Θ which is the set of particles of different resolution and different fluid type as m. Subsequently, a normal vector $\hat{\mathbf{n}}_c = \nabla c_m \,/\, |\, \nabla c_m \,|$ is computed.

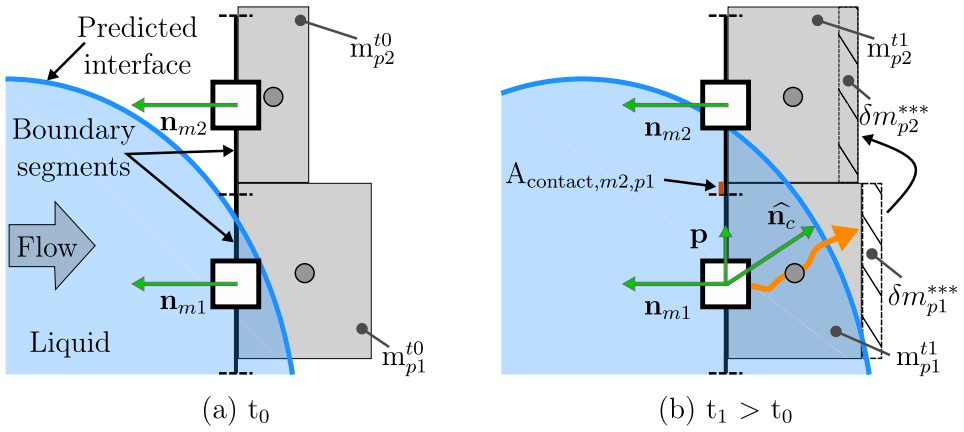

Fig. 12. Mass incrementation of coarse gaseous boundary particles near the fine-resolution predicted phase interface due to the CGMI.

In Fig. 12(b), this normal vector was calculated for the gaseous marker m_1, pointing away from the liquid fragment, and hence, into the gaseous phase. With the face normal of the boundary segment, or marker, $\mathbf{n}_m$, a boundary-parallel vector is calculated:

$$\mathbf{p} = \widehat{\mathbf{n}}_c - \mathbf{n}_m\left(\mathbf{n}_m \cdot \widehat{\mathbf{n}}_c\right). \tag{21}$$

Subsequently, the color-gradient mass increment (CGMI) is calculated at the marker m_1 of the phase χ in vicinity of the phase interface and passed along the boundary in the direction of $\mathbf{p}$ to m_2, belonging to the same phase χ:

$$\delta m_{m1,CGMI} = -\|\mathbf{p}\|\, m_{p1}\, \xi_{CGMI} = -\delta m_{m2,CGMI}. \tag{22}$$

This mass increment scales with the length of $\mathbf{p}$ and the mass of the particle p_1 that would otherwise cause a phase encapsulation in the opposite phase if it was released. ξ_{CGMI} is chosen to be 0.1, so that at maximum 10 % of a boundary particles mass is moved per timestep. The marker mass increment is then distributed over only the closest associated particle. In this description, in case of the markers m_1 and m_2, just the particles p_1 and p_2, respectively:

$$\delta m_{p1,CGMI}^{***} = \delta m_{m1,CGMI}, \tag{23}$$

$$\delta m_{p2,CGMI}^{***} = \delta m_{m2,CGMI} = -\delta m_{p1,CGMI}^{***}, \tag{24}$$

and the update of the masses of particles in contact with the boundary is then:

$$m_p^{n+1} = m_p^n + \underbrace{\delta m_p^* + \delta m_p^{**} + \delta m_{p,CGMI}^{***}}_{\delta m_p}. \tag{25}$$

The particles position is then corrected using the updated particle mass m_p^{n+1} in Eq. (17).

As this computation is conducted for all markers in vicinity to the phase interface, a gaseous mass increment calculated inside of a liquid fragment is passed parallel to the boundary into the other fluid, where it is manifested as a gaseous particle instead of a gas inclusion. The procedure is in an analogous way conducted for liquid boundary particles in the surrounding gas. At the end, the phases at the interface are more clearly separated. As mass increments are shifted along the boundary, the total mass of a subdomain remains unchanged.

4. Validation

In this Section, various test scenarios are discussed in order to demonstrate the capability of the framework for multi-phase flows. The first single-phase test case is that of a lid-driven cavity to be presented in Section 4.1. This configuration imposes simultaneously an entry and an exit of flow within the refinement zone, fostering dynamic evaluations. The next test case is that of a Taylor–Green flow (cf. Section 4.2), which, due to the absence of external forcing, is well suited for studying long-term effects. This is followed by a Kelvin–Helmholtz instability (cf. Section 4.3). Many multi-phase flows are driven by instabilities, and so is atomization. A multi-resolution approach needs to be capable to predict these instabilities without triggering any further disturbances of the phase interface. Although two materials are involved, they share the same material properties. In the test case, a fluid type or phase identifier is used to distinct between the two materials. This configuration is therefore often referred to as a “single-phase” Kelvin–Helmholtz instability and convergence can be achieved with a lower computational effort, compared to a real two-phase scenario. The last canonical test case in Section 4.4 is focussed on a real multi-phase flow. An oscillating droplet is passing through regions of different resolution levels. The goal is to demonstrate the capability of our approach to capture a multi-phase flow with realistic material properties. Further, it is shown that the influence of the transition to another resolution level does not cause inaccuracies. Finally, as a highlight, this section concludes with a demonstration of the multi-resolution approach in an application-relevant generic atomization case (cf. Section 4.5).

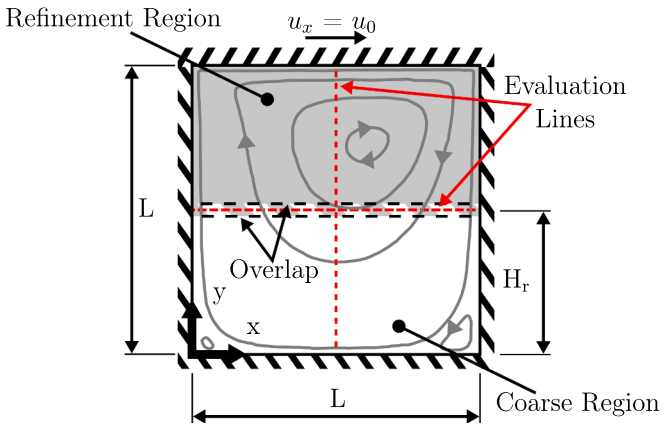

Fig. 13. Sketch of the Lid-Driven Cavity with streamlines extracted from Ghia et al. [57]. The refinement region is located at the upper part of the domain.

Table 1
Uniform and multi-resolution (MR) simulation cases.

Case	L/dx_{min}	L/dx_{max}	Number of particles
L50	$L/50 = 0.02\,m$	–	3,400
L100/50 MR	$L/100 = 0.01\,m$	$L/50 = 0.02\,m$	9,500
L100	$L/100 = 0.01\,m$	–	12,000
L200/100 MR	$L/200 = 0.005\,m$	$L/100 = 0.01\,m$	31,500
L200	$L/200 = 0.005\,m$	–	43,000

4.1. Lid-driven cavity

The lid-driven cavity is a popular test case for single-phase flow analysis. This benchmark case including a prominent vortex formation is depicted in Fig. 13. The objective of this benchmark is to validate the ability of our approach to predict single-phase flows. The distinct flow structure enables an in-depth assessment of the internal boundaries, as the streamlines cross the interface of the different spatial resolution regions at varying angles from perpendicular to parallel. This methods ability to handle a non-perpendicular flow across the interface between coarse and fine resolution and the potential use in an arbitrarily shaped refinement zone is demonstrated. Five simulations are performed, comprising three uniform cases (L200, L100, L50) and two multi-resolution cases (L200/100 MR and L100/50 MR). For the multi-resolution simulations, the mean particle distances are different in the top and bottom half of the computational domain. This is indicated by the gray shading. As outlined previously, our method always requires an overlap, where the two solutions coexist. In the sketch, the overlap region is indicated by the dashed lines. The refinement region starts roughly at $H_r = 0.5L$ and extends by half the overlap-size to the bottom. There are two evaluation lines at the middle of the length or height of the domain, which divide the computational domain into 4 quadrants. Reference results from Ghia et al. [57] will be used to evaluate the accuracy of the predictions.

The cavity consists of a square with a side length L of 1 m. It is filled with a single fluid of reference density $\rho_0 = 1\,kg\,m^{-3}$, viscosity $\mu = 1\,kg\,m^{-1}\,s^{-1}$ and speed of sound $c = 10\,m\,s^{-1}$. The lid moves with $u_0 = 1\,m\,s^{-1}$ to the right, the Reynolds number and the artificial Mach number amount to 100 and 0.1, respectively. The mean particle spacings of the simulations are summarized in Table 1. The multi-resolution simulations contain two particle spacings.

In Fig. 14 contour plots of the velocity field are presented. At the center the multi-resolution simulation is shown. On the left the uniform L200, and on the right the uniform L100 resolution are shown. Additionally, the contour plots of the uniform resolutions contain white contour lines taken from the multi-resolution prediction to enhance comparability. Furthermore, the red evaluation lines at $y_+ = y/L = 0.5$ and $x_+ = x/L = 0.5$ dividing the domain into 4 quadrants are depicted. For the multi-resolution simulation, also the overlap region is illustrated.

From the top right corner, the fluid is moving downwards and then redirected by the bottom right and then bottom left corner. A vortex is formed which is centered in the upper right quadrant, with minimal velocity magnitudes at its center. It is extending downwards, causing a parallel flow at the intersection of the evaluation lines ($y_+ = x_+ = 0.5$). Closer to the left and right walls, the fluid is crossing the internal boundary in a perpendicular direction. In this scenario, the transition zone has to cope with the full range of possible flow angles.

Comparing the black and white contour lines of the left plot, it is evident that the agreement with the uniform L200 simulation in the top quadrants is nearly perfect. There is only a slight deterioation below the overlap in the bottom quadrants. However, the solution in the bottom two quadrants of the multi-resolution simulation was predicted using particles corresponding to the L100

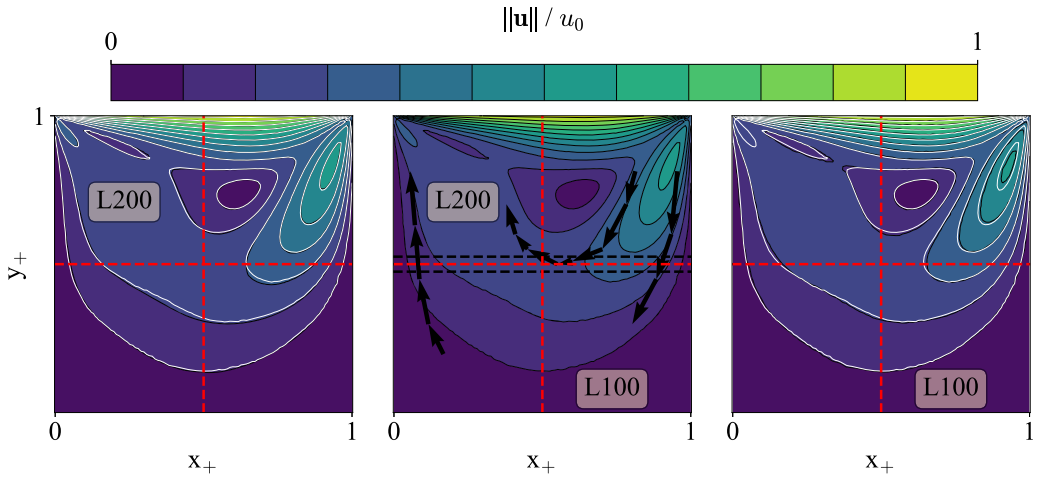

Fig. 14. Contour plots of the stationary velocity magnitude at $t_+ = 100$. Predictions with uniform fine (left), multi-resolution (center) and uniform coarse (right) resolutions are shown. White contour lines correspond to the multi-resolution result.

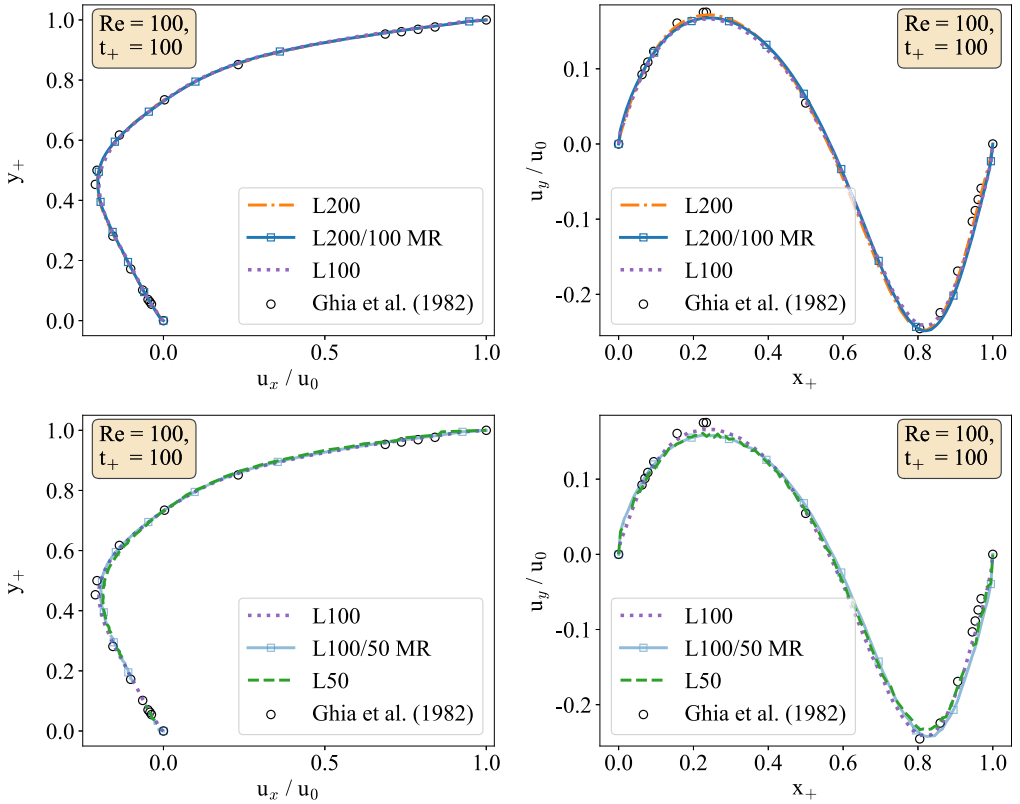

Fig. 15. Comparison of horizontal (left column) and vertical (right column) velocity profiles with reference results of Ghia et al. [57]. The top row shows the fine-resolution comparison (L200 vs. L200/100 MR vs. L100), while the bottom row presents the coarse-resolution comparison (L100 vs. L100/50 MR vs. L50).

resolution. As expected, comparing those quadrants with the uniform L100 simulation again yields a good agreement. Hence, the multi-resolutional results are in visual agreement with both reference simulations.

In Fig. 15 the stationary velocity profiles at $t_+ = tc_0/L = 100$ along the evaluation lines are depicted. Reference results are taken from Finite-Difference predictions of Ghia et al. [57], computed on a mesh with uniform cell sizes. It is evident, that the overall agreement of the uniform simulations L200, L100 and L50, as well as the corresponding multi-resolution simulations L200/100 MR and L100/50 MR is good. We conclude, that the multi-resolution approach is reproducing this single-phase flow.

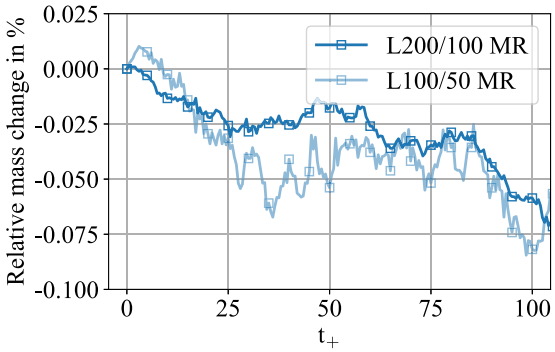

Fig. 16. Evolution of the mass for the multi-resolution simulation.

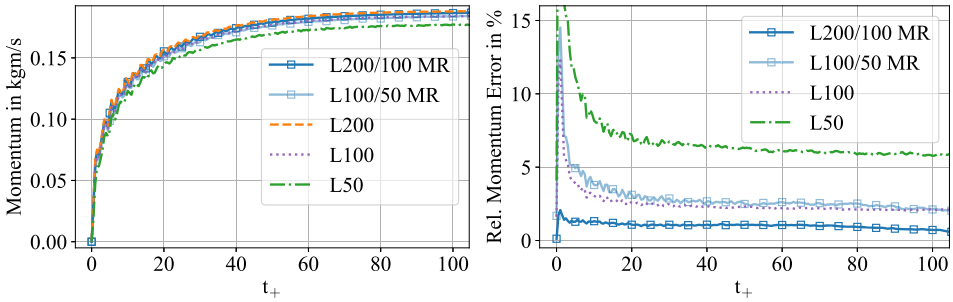

(a) Evolution of the total momentum. (b) Deviation relative to L200.

Fig. 17. Time history of the total momentum and the deviation from the uniform fine simulation.

The quality of the numerical results produced by a domain-coupling approach strongly depends on its capability to conserve mass and momentum. Hence, in the following, different evaluations will be carried out to assess the quality of the methodology with regard to its conservation characteristics. The total mass loss over time is depicted in Fig. 16. An almost linear reduction of the mass is evident. The total loss amounts to 0.7 ‰ at the end of the simulations. A mass loss like this is to be expected and remains well within or below the values reported in other documented works [25,55].

In Fig. 17(a) the total momentum evolution over time is depicted. It is evident, that the overall agreement of the uniform simulations L200, L100 and L50, as well as the corresponding multi-resolution is again good. Differences become apparent when evaluating the relative momentum error with respect to the uniform L200 simulation (cf. Fig. 17(b)). In this comparison, the deviations of the multi-resolution simulations follow the qualitative trend of their respective uniform counterparts, while their quantitative error levels consistently fall between the two corresponding uniform resolutions, as expected for their effective resolution.

4.2. Taylor–Green flow

As second benchmark, the laminar Taylor–Green vortex at Reynolds number $Re = 100$ is investigated. The absence of external forcing avoids a possible compensation of errors and instead, it supports the accumulation of errors, making the test case particularly sensitive to adverse effects of the multi-resolution scheme. This allows a clear assessment of the capabilities of the multi-resolution scheme to capture the essential flow features and controlling numerical errors. The dimensions of this case are given by $(x,y) \in [0,L]^2$, with $L = 1\,\mathrm{m}$. All external boundaries are periodic. Inside the square computational domain quadratic refinement zones with edge length of $0.4\,L$ are applied. Two uniform resolutions are considered, $L/dx = 200$ and $L/dx = 100$, along with the multi-resolution variant L200/100 MR, corresponding to 40,000, 10,000, and 18,100 particles, respectively. The multi-resolution case is examined in three configurations: located in the top right corner, in the center, and in the bottom left corner. In Fig. 18, only the refinement zone in the top right corner depicted. The flow is initialized as

$$\begin{aligned} U_x &= -U_0 \exp(bt) \cos(2\pi x) \sin(2\pi y), \\ U_y &= U_0 \exp(bt) \sin(2\pi x) \cos(2\pi y), \end{aligned} \tag{26}$$

with $t = 0$, the decay rate $b = -8\pi\mathrm{Re}$ and the initial velocity $U_0 = 1\,\mathrm{m\,s^{-1}}$. The density ρ set to 1, and the speed of sound $c = 10\,\mathrm{m\,s^{-1}}$. The individual refinement regions are defined by: $(x_{\mathrm{bottom}}, y_{\mathrm{bottom}}) \in [0.05\,L, 0.45\,L]^2$, $(x_{\mathrm{center}}, y_{\mathrm{center}}) \in [0.30\,L, 0.70\,L]^2$ and $(x_{\mathrm{top}}, y_{\mathrm{top}}) \in [0.55\,L, 0.95\,L]^2$.

In Fig. 19 the decay of the normalized total kinetic energy $E_{\mathrm{kin},+} = E_{\mathrm{kin}}/E_{\mathrm{kin},0}$ and its deviation from theory is depicted. To enhance visual clarity and avoid overcrowding of the decay plot (cf. Fig. 19(a)), only the multi-resolution simulation with the largest (yet

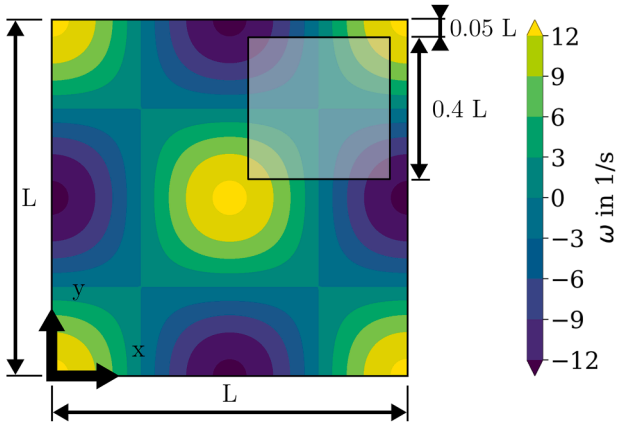

Fig. 18. Sketch of the Taylor–Green Flow with a vorticity contour plot depicting the vortices including a single quadratic refinement zone in the top right corner for time instance $t = 0$.

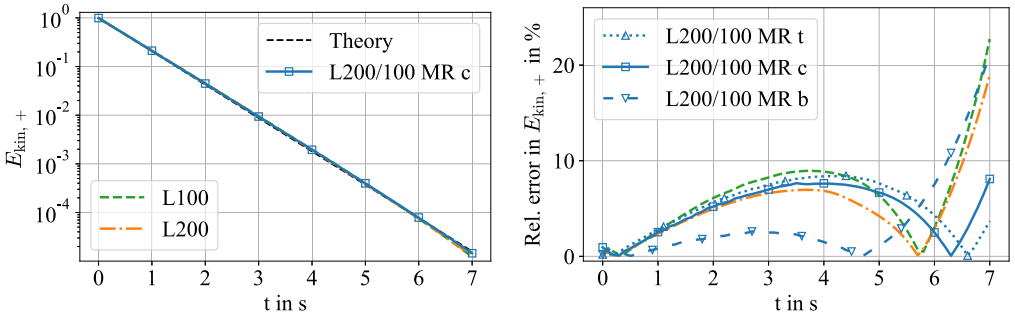

(a) Kinetic Energy Decay (b) Deviation from Theory

Fig. 19. Time history of the total kinetic energy and its deviation from the theoretical solution.

still minor) deviation is presented alongside the two reference solutions. The multi-resolution simulation shows excellent agreement with the kinetic energy decay of the uniform simulations as well as the theoretical decay. The evaluation of the Taylor–Green flow is carried out up to t = 7 s. Since numerical errors tend to accumulate over time, maintaining agreement with reference data over such a long time span is a particularly strong indicator of numerical accuracy and robustness. Also the deviation from the theoretical energy decay depicted in Fig. 19(b)) is well within limits of the uniform fine and coarse simulations, essentially showing very similar qualitative and quantitative behavior.

Finally, contour plots of the vorticity (left column) and normalized pressure (right column) are depicted in Fig. 20. For the coarser resolution L100, the vorticity and pressure fields are strongly influenced by small-scale noise, which is particularly visible at the contour boundaries. This is significantly improved in the uniform fine resolution L200. To accurately capture the spatial distribution of the vorticity field, particular attention must be paid during post-processing. Classical SPH-based approximations tend to suppress small-scale velocity fluctuations [58]. To mitigate this effect, we interpolated the velocity field onto a Cartesian grid and computed the vorticity using second-order central finite differences, thereby preserving most of the small-scale noise in the post-processed data. This small-scale noise remains visible at the highest resolution, albeit at lower levels compared to coarser resolutions. Notably, the noise level within the refinement zone of the L200/100 MR configuration is also reduced – for instance, at x/L = y/L = 0.25, where a sign change produces a cross pattern that is more accurately captured with the L200 resolution than with L100. This demonstrates the effectiveness of the refinement approach.

4.3. Kelvin–Helmholtz instability

Until now, only single-phase benchmarks have been examined. The primary strength of the proposed framework, however, lies in its ability to accurately predict multi-phase flows. Among the limited number of multi-phase test cases that exhibit convergence using SPH, the Kelvin–Helmholtz instability is a suitable case for this work. This phenomenon is also of particular relevance to shear-driven atomization processes. As such instabilities are very sensitive to factors like resolution, initial particle distribution and many more, errors caused by the refinement zone are expected to trigger additional perturbations of the phase interface. Hence, the goal of this test case is to determine the effect of a refinement zone on triggering or amplifying instabilities. This benchmark is based on the studies of Lecoanet et al. [59] and Tricco [60]. The findings from the SPH simulations conducted by Tricco [60] are summarized

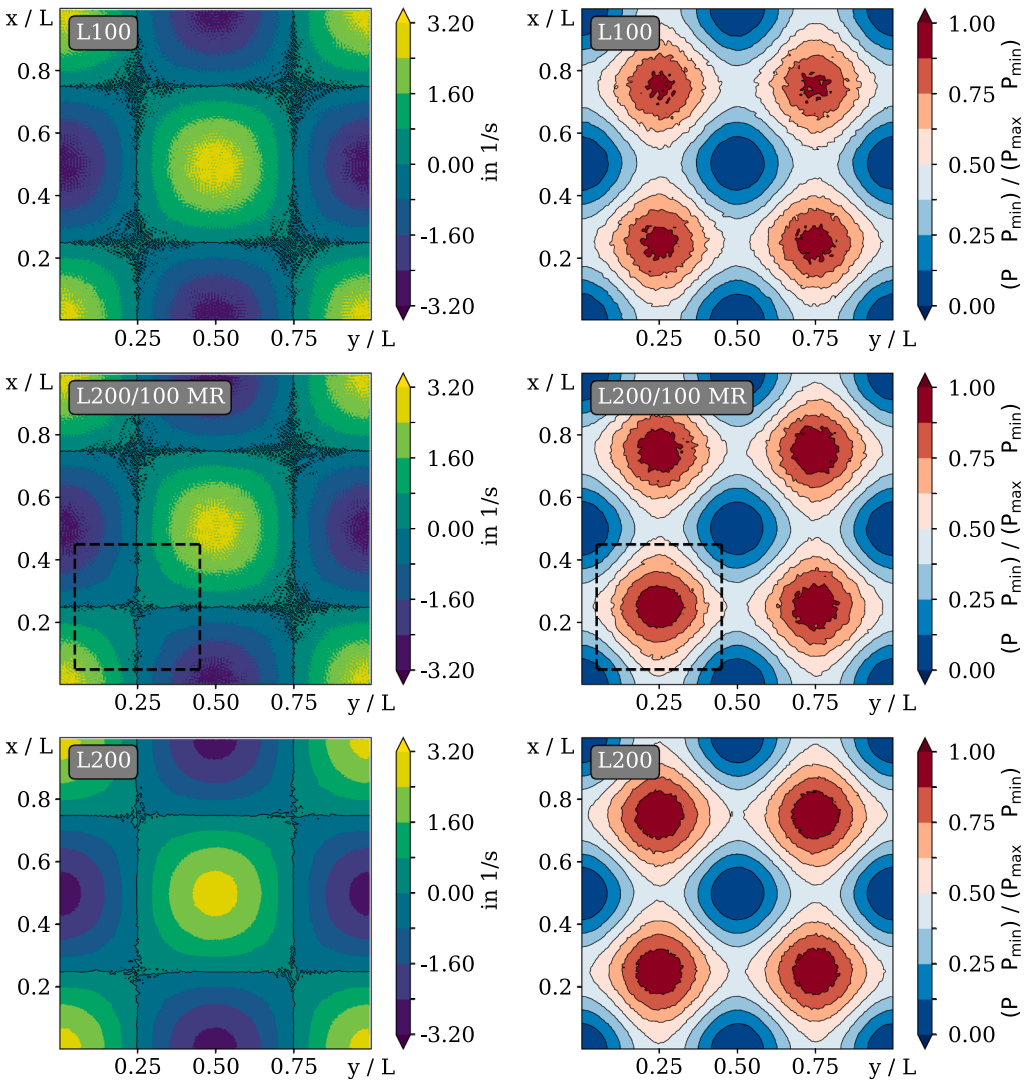

Fig. 20. Comparison of vorticity (left) and normalized pressure contours (right) at t = 2 s for the uniform simulations L200 (top) and L100 (bottom), and for the multi-resolution variant L200/100 MR (center).

below, culminating in our numerical setup for this case (cf. Fig. 21). For this benchmark, two fluids with identical material properties are considered, and hence, a convergent result is to be expected for resolutions at more than $N_x = 1024$ particles along the shorter edge of the domain. However, major parts of the instability can already be reproduced with $N_x = 128$ particles. In order to reduce the noise within the winding phase interfaces, a greater kernel support has proven to be beneficial [60]. Hence, we apply the pairing-stable Wendland C4 kernel for this benchmark. The radius of the kernel support is taken as 4.8 times the mean particle distance. The application of *tensile instability control* is particularly beneficial in the low-pressure regions that form inside the vortex cores, where it contributes to preserving well-defined interfaces. For interfacial flows, repulsive contributions to the regular particle shifting are deactivated (cf. Eqs. (5) and (6), $\xi_{\text{Rep}} = 0$).

The dimensions of this test case are $L_x = 1\,\text{m}$ and $L_y = 2\,\text{m}$. Two configurations of the refinement region are investigated, one with the internal boundaries parallel to the upper interface (Fig. 21(a)) and one with the additional internal boundaries perpendicular to the lower interface (Fig. 21(b)). The parallel refinement region is between $y_{r,1} = 1.18\,\text{m}$ and $y_{r,2} = 1.82\,\text{m}$. Dimensions of the lower refinement are given by $x_{r,3} = 0.27\,\text{m}$, $x_{r,4} = 0.73\,\text{m}$, $y_{r,3} = 0.18\,\text{m}$ and $y_{r,4} = 0.82\,\text{m}$. The bottom phase interface is at $y_1 = 0.50\,\text{m}$ and the top interface at $y_2 = 1.50\,\text{m}$. The resolutions for this benchmark vary between $N_{x,\text{coarse}} = 128$, $N_{x,\text{medium}} = 256$ and $N_{x,\text{fine}} = 512$ particles along L_x (cf. Table 2). In case of the perpendicular configuration, the regular refinement ratio of 4 is used. The positioning of the internal boundary in case of the parallel configuration allows for the more optimistic refinement ratio of 16. Hence, the multi-resolution simulation applies either the N128 and N512 or N256 and N512 resolutions, depending on the configuration. The density, viscosity, and speed of sound used in this test case are $1\,\text{kg}\,\text{m}^{-3}$, $2 \times 10^{-5}\,\text{Pa}\,\text{s}$ and $20\,\text{m}\,\text{s}^{-1}$, respectively. Based on the relative velocity $\Delta u = 2\,u_0 = 2\,\text{m}\,\text{s}^{-1}$, the Reynolds number amounts to 10^5 and the Mach number to 0.1. Smooth velocity profiles

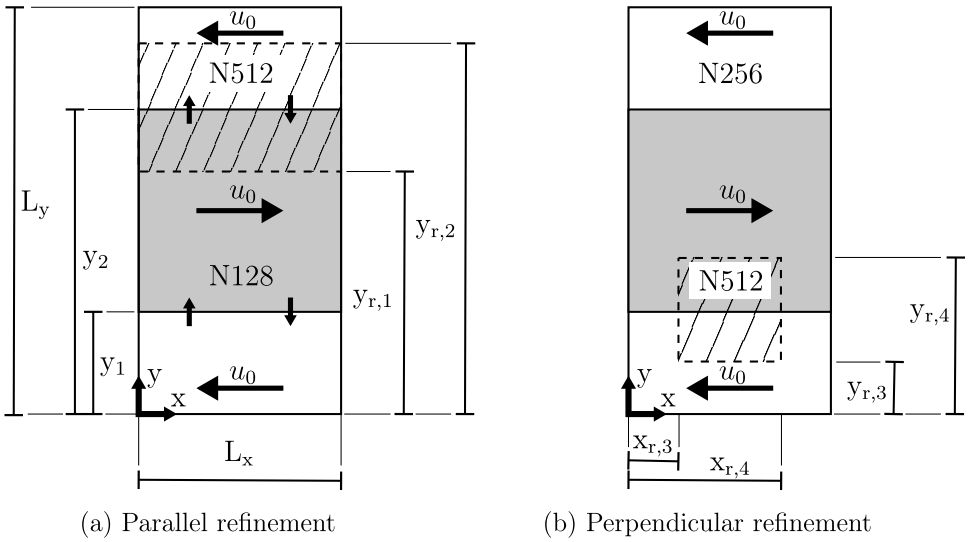

Fig. 21. Sketch of the Kelvin–Helmholtz instability. The dominant instability is seeded at the phase interface through vertical velocity perturbation. Two configurations for the refinement are shown.

Table 2
Uniform and multi-resolution (MR) simulations.

Case	$N_{x,max}$	$N_{x,min}$	Number of particles	Resolution levels	Configuration
N128	128	–	32,800	1	–
N256	256	–	131,000	1	–
N512/128 MR	512	128	211,200	2	Parallel
N512/256 MR	512	256	216,700	2	Perpendicular
N512	512	–	524,300	1	–

are imposed:

$$U_x = U_0\left[\tanh\left(\frac{y-y_1}{0.05}\right) - \tanh\left(\frac{y-y_2}{0.05}\right) - 1\right],$$
$$U_y = U_I \sin(2\pi x)\left[\exp\left(-\frac{(y-y_1)^2}{0.04}\right) + \exp\left(-\frac{(y-y_2)^2}{0.04}\right)\right], \tag{27}$$

with a perturbation velocity $U_I = 0.01\,\mathrm{m\,s^{-1}}$.

In Fig. 22(a)–(d) the evolving fluid interfaces are shown for multiple time instants. For all time instants, in the two left quadrants, the simulation with two resolution levels is depicted. The upper quadrant illustrates the finer resolution near the interface, transitioning to coarser particles at greater distances. The dashed lines encompass the region of higher resolution. Since in the multi-resolution simulation, the upper interface is resolved by particles of the mean particle distance L_x / 512, the reference solution to this is the uniform N512 simulation depicted in the upper right quadrant of each time instant. The bottom two quadrants yield the interface resolved by particles of the sizes L_x / 128, with the uniform N128 simulation on the right.

It is evident, that the multi-resolution simulation is capable to reproduce the reference result in the refined as well as the derefined region. This remains true even for the latest of the depicted time instant in Fig. 22(d), with only marginal differences to the reference result. At $t = 4.0\,\mathrm{s}$, even at the highest resolution presented (N512), the thinnest filaments appear disrupted, as they are only a few particles thick and therefore cannot be reliably resolved. Rounded, bubbly structures emerge. This effect is even more pronounced at the coarsest resolution presented (N128), where no fine, continuous filaments form, and only thick, rounded filament ends remain. The effect diminishes as the structures grow larger relative to the kernel support–underscoring the need for even higher resolutions than N512 to faithfully capture the Kelvin–Helmholtz instability with SPH [60].

In Fig. 23 characteristic metrics of this instability are compared. The multi-resolution model again shows excellent agreement with the reference results for both, amplitude growth rate and density-specific kinetic energy. The linear growth phase (0.5 s to 1.5 s) is perfectly predicted, matching the expected slope of $\exp(\pi t)$.

In the configuration discussed previously, the refinement zone was optimally positioned: the resolution was increased near the interface, while the internal boundary was placed farther away in regions with weaker gradients, thereby avoiding any potential adverse effects on the simulation. This reflects the ideal use of multiple refinement levels in multi-phase flows. It particularly improves the computation of the Kelvin–Helmholtz instability and resulted in a speed-up by a factor of 2 compared to a uniform fine resolution

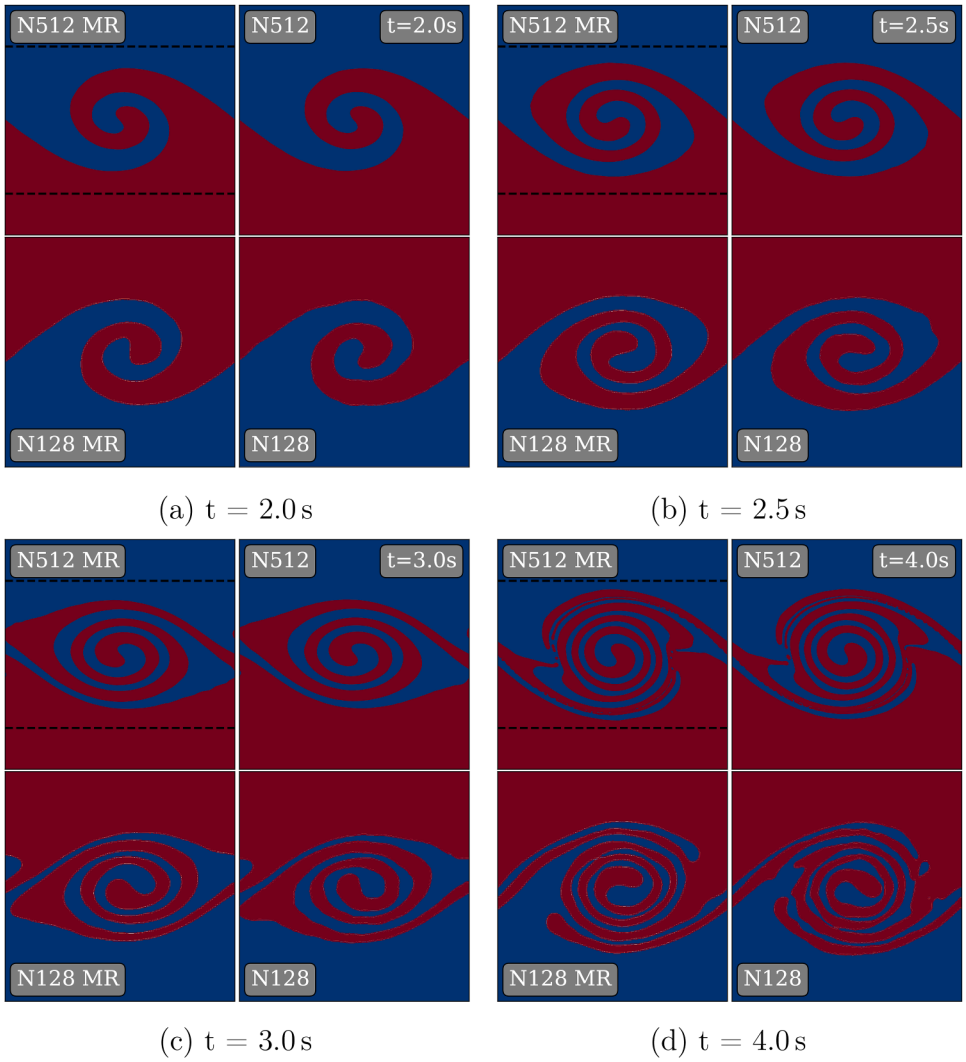

Fig. 22. Comparison of the evolving interfaces for the multi-resolution case N512/128, the uniform case N512 and the uniform N128 prediction. For all time instants, the multi-resolution simulation N512/128 MR is depicted in the left two quadrants. The uniform N512 prediction is in the top right quadrant and the uniform N128 prediction in the bottom right quadrant.

(N512U in Fig. 24). The multi-resolution configuration (N512MR) corresponds to an effective particle number equivalent to a uniform discretization with $N_x = 325$ (N325U), which represents the theoretical upper limit of possible relative speed-up – accounting only for the amount of particles and neglecting algorithmic overhead. Hence, this estimate does not account for additional costs associated with maintaining multiple interaction lists, interpolating guards and other additional particle types or any other implementation-specific complexities.

In contrast, the following configuration deliberately places the refinement zone in the most detrimental way. As a result, the interface must repeatedly traverse the internal boundary, allowing for a detailed investigation of any adverse effects associated with this process. This corresponds to the perpendicular configuration of the refinement zone in Fig. 21(b). The internal boundaries are expected to introduce microscopic perturbations. To compensate for this and ensure that the physical instability remains dominant, the velocity perturbation U_I is increased to $0.05\,\mathrm{m\,s^{-1}}$, which effectively corresponds to observing the simulation at a later stage. Therefore, time instances t^* of the simulation results are shifted, such that the linear growth regime coincides with that of the previously investigated configurations (cf. Fig. 23, perpendicular configuration). Restricting Shepard interpolation to the same fluid (cf. Eq. (8)) would result in a partially filled kernel support at the interface. Therefore, cross-fluid interpolation is permitted in this case. However, this approach is generally discouraged - particularly when different material properties are involved. Comparable accuracy could instead be achieved by employing higher-order interpolation schemes.

The snapshots of the phase interfaces are given by Fig. 25. As indicated earlier, the unrefined interface region, located far from the refinement zone, remains unaffected and is therefore omitted. Only the relevant lower interface is shown. The left column displays

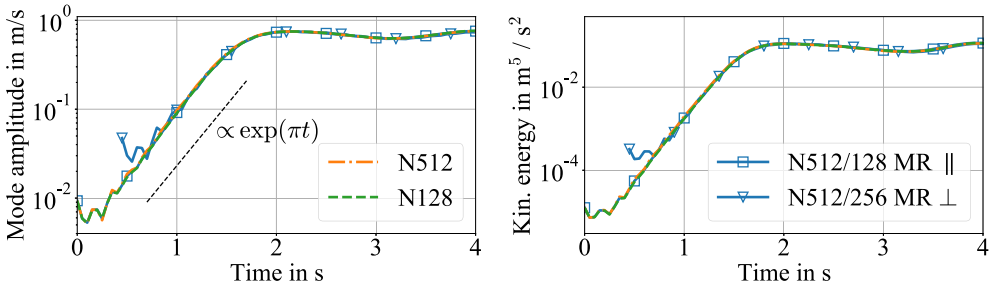

Fig. 23. Comparison of characteristic metrics of the Kelvin–Helmholtz benchmark. Left: Mode amplitude. Right: Density-specific kinetic energy.

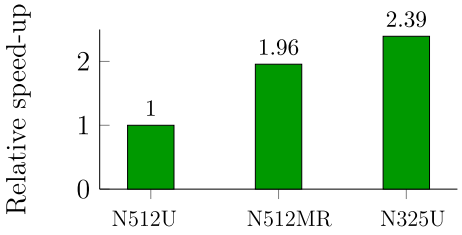

Fig. 24. Comparison of relative performance. Values represent the inverse wall time normalized by the uniform fine simulation.

Table 3
Uniform and multi-resolution (MR) simulations used to show resolution behavior.

Case	$N_{x,max}$	$N_{x,min}$	Number of particles	Resolution levels	Configuration
N256/128 MR	256	128	57,700	2	Perpendicular
N512/256 MR	512	256	216,700	2	Perpendicular
N1024/512/256 MR	1024	256	626,900	3	Parallel & perpendicular
N1024	1024	–	2,097,200	1	–
N1024 VoF	1024	–	2,097,200 cells	1	–

results for the uniform medium resolution of $N_{x,medium} = 256$. The central columns show the multi-resolution simulations, one with reconstruction algorithms activated (center left), and one with reconstruction deactivated (center right). The right column corresponds to the uniform fine simulation of $N_{x,fine} = 512$.

It is evident, that activating the reconstruction algorithms distinctly improves the shape of the interface. When omitting the reconstruction, the interface resembles the reference only during the initial two time instances. At later times, the interface becomes strongly diffused, and the original vortex structure is unrecognizable. In contrast, activating the reconstruction algorithms preserves the expected shapes throughout the simulation. A comparison of the final time instance between the uniform medium resolution and the multi-resolution simulation with reconstruction (leftmost two columns) reveals improved preservation of fine-scale structures in the multi-resolution case. These structures tend to degrade into circular patterns at lower resolution, but are better resolved by the multi-resolution scheme. Based on these findings, it is safe to conclude, that the internal boundaries will not affect the phase interface and no additional instabilities will be triggered, if the reconstruction schemes are applied.

For the final test for this benchmark, we increase the resolutions applied to up to 1024 particles along the shorter edge. To reduce total computation time, the velocity perturbation U_I is increased to $0.10\,\mathrm{m\,s^{-1}}$. Time instances are again shifted and denoted with t^{**}. In total, we extend the simulation design space to include the following simulations reported in Table 3. The finest multi-resolution simulation considered, N1024/512/256 MR, employs a special configuration that combines parallel and perpendicular refinement levels (cf. Fig. 21) to achieve a substantial reduction in computational cost. Starting from a base resolution of N256, the resolution is first doubled to N512 within the region $y_{N512} \in [0.06\,\mathrm{L}, 0.94\,\mathrm{L}]$. A further refinement to N1024 is then applied in the confined area $x_{N1024} \in [0.25\,\mathrm{L}, 0.75\,\mathrm{L}]$ and $y_{N1024} \in [0.16\,\mathrm{L}, 0.84\,\mathrm{L}]$.

The resulting inner vortex of the lower interface at $t^{**} = 2.0\,\mathrm{s}$ for the different resolutions is shown in Fig. 26. Multi-resolution predictions with increasing resolution are represented by progressively darker shades of blue. The uniform N1024 result is shown as a solid black line, while a reference prediction obtained with the Volume of Fluid (VoF) method is depicted by the dashed line, using the interIsoFoam solver of the *OpenFOAM* package.

As is evident, the highest-resolved simulations – the uniform SPH prediction (N1024) and the VoF reference (N1024 VoF) – show very good agreement at this resolution. Even the coarsest multi-resolution case, N256/128 MR, is able to capture the inner vortex shape reasonably well, although initial interface disturbances are still visible and affect the agreement with finer resolutions. These discrepancies gradually diminish, and convergence toward the reference results becomes evident with increasing resolution of the multi-resolution cases.

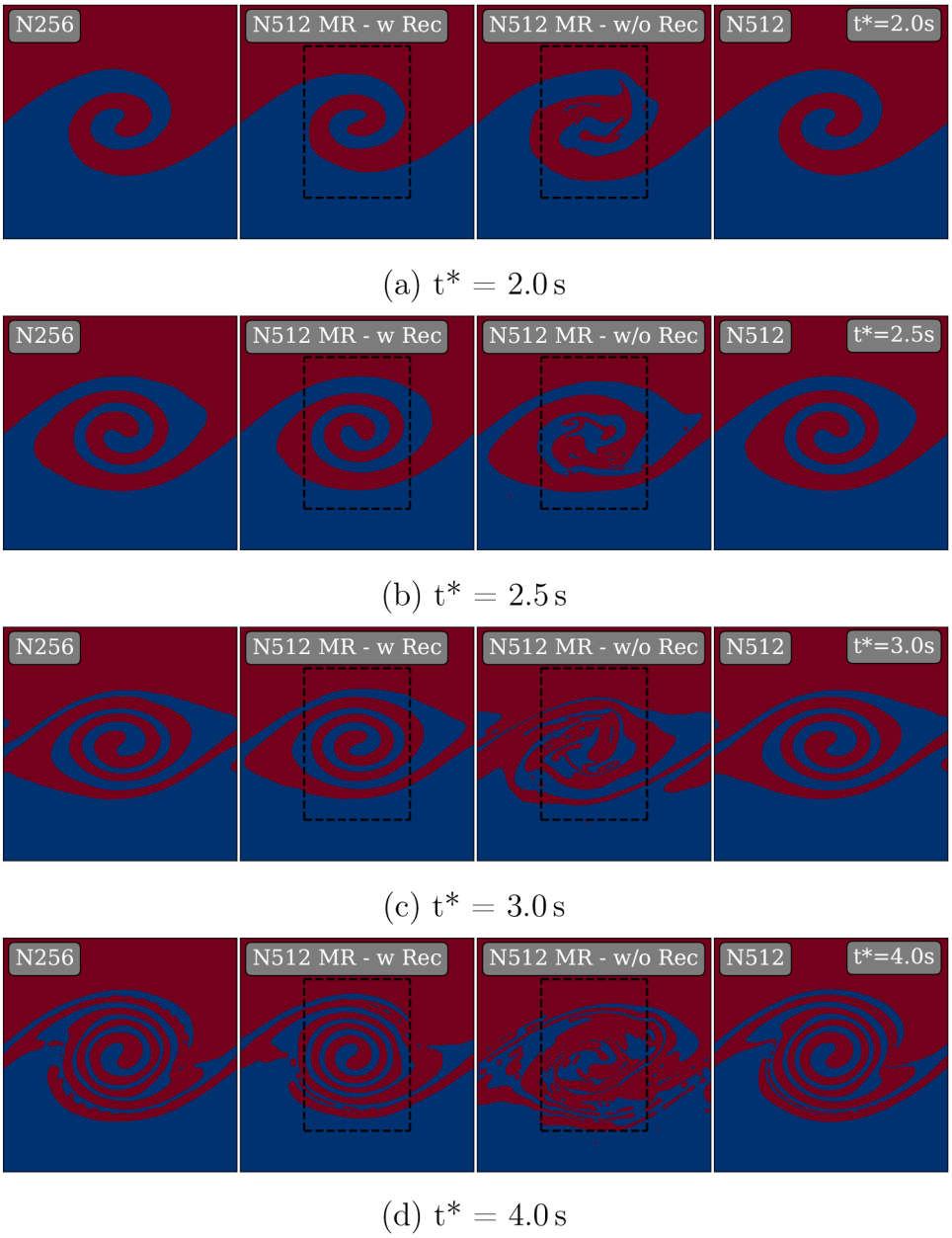

Fig. 25. Comparison of the evolving interfaces for a refinement zone with internal boundaries perpendicular to the phase interface. Left column corresponds to uniform medium resolution, center columns to multi-resolution with and without reconstruction, right column to uniform fine resolution.

4.4. Oscillating droplet

The capability of the framework to handle interfacial flows with realistic material properties is investigated. A suitable test case is an oscillating droplet moving across regions of different resolution levels. This benchmark case is usually conducted to demonstrate the validity of the surface tension model. Since multi-phase flows are often driven by surface tension effects, the modeling of surface tension is of great importance. In this work, the benchmark is used to demonstrate that the effect of the transition to another resolution level on surface tension driven phenomena is negligible. Further, it will be shown, that the characteristics of a moving droplet is not compromised.

The numerical domain of this case is depicted in Fig. 27. In this test case a high density ratio of 100 is considered, which corresponds to compressed air and water. The material parameters are chosen to reflect realistic material behaviour in technical applications for two-phase flows such as atomization. The reference density of the gas is set to $9.95\,\mathrm{kg\,m^{-3}}$ and that of the liquid to $1000\,\mathrm{kg\,m^{-3}}$. The viscosities are $0.034\,\mathrm{mPa\,s^{-1}}$ and $2.93\,\mathrm{mPa\,s^{-1}}$ for the gas and liquid, respectively. The surface tension between gas and liquid

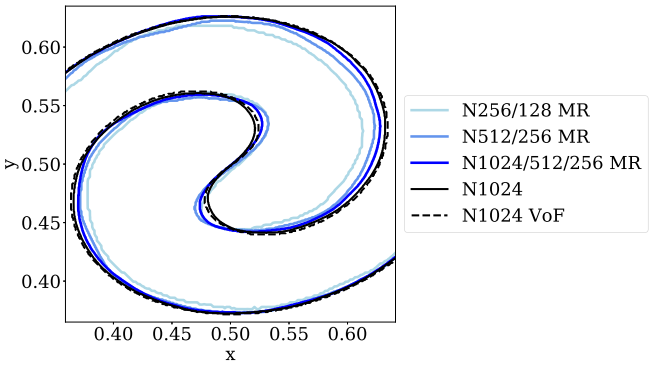

Fig. 26. Fluid interfaces with increasing resolution for time instance t** = 2.0 s.

Table 4
Simulation Cases with resolution and number of particles (total / droplet).

Case	dx_{min}	dx_{max}	Number of particles	Number of liquid particles (t = 0)
10.0	10.0 µm	–	14,000	158
5.0/10.0 MR	5.0 µm	10.0 µm	34,500	628
5.0/7.5 MR	5.0 µm	7.5 µm	42,700	628
5.0	5.0 µm	–	53,000	628
2.5/5.0 MR	2.5 µm	5.0 µm	128,700	2501
2.5	2.5 µm	–	206,000	2501

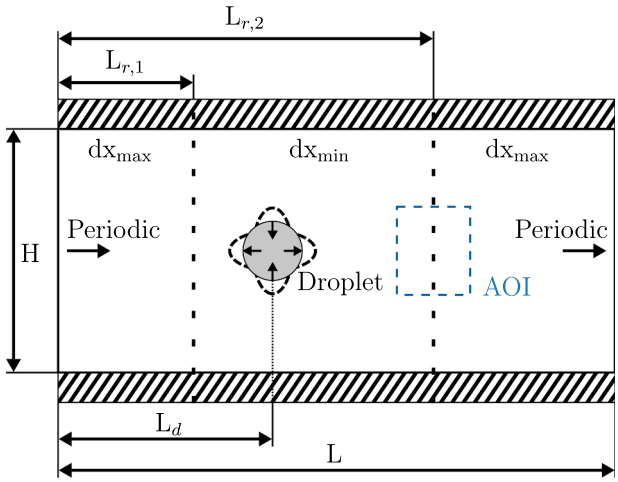

Fig. 27. Sketch of an oscillating droplet transitioning from fine to coarse. The area of interest (AOI) is where the droplet moves through the transition region.

amounts to $\sigma = 0.07\,\mathrm{N\,m^{-1}}$. The artificial speed of sound is set to $150\,\mathrm{m\,s^{-1}}$ for the gas, and for the liquid to $15\,\mathrm{m\,s^{-1}}$. For an accurate reconstruction of the local shape of the interface a smaller kernel can be of advantage. Therefore, the quintic spline kernel is used for these calculations, enabling the ratio of $h/dx = 1$ in both resolution levels.

The droplet and its surrounding gas flow are initialized with a mean axial velocity of $2.5\,\mathrm{m\,s^{-1}}$. In order to trigger the second mode of oscillation [61], we add a relative velocity onto the droplet [34]:

$$U_x = U_0 \frac{x}{R}\left(1 - \frac{y^2}{Rr}\right)\exp\left(-\frac{r}{R}\right), \tag{28}$$

$$U_y = -U_0 \frac{y}{R}\left(1 - \frac{x^2}{Rr}\right)\exp\left(-\frac{r}{R}\right), \tag{29}$$

with a velocity amplitude U_0 of $2.5\,\mathrm{m\,s^{-1}}$. The oscillating droplet is then convected through a channel of height $H = 0.5\,\mathrm{mm}$ and length $L = 2.5\,\mathrm{mm}$. At the beginning of the simulation, the droplets center is located at $L_d = 0.5\,\mathrm{mm}$. In the multi-resolution simulations, at $L_{r,1} = 0.2\,\mathrm{mm}$ the minimum resolution of dx_{min} commences, and ends at $L_{r,1} = 1.0\,\mathrm{mm}$. Everywhere else, the maximum resolution dx_{max} is utilized. All simulated cases are listed in Table 4. Another special case, the 5.0/7.5 MR setup, represents a second deviation from the default refinement ratio of 4. Here, the ratio corresponds to 2.25.

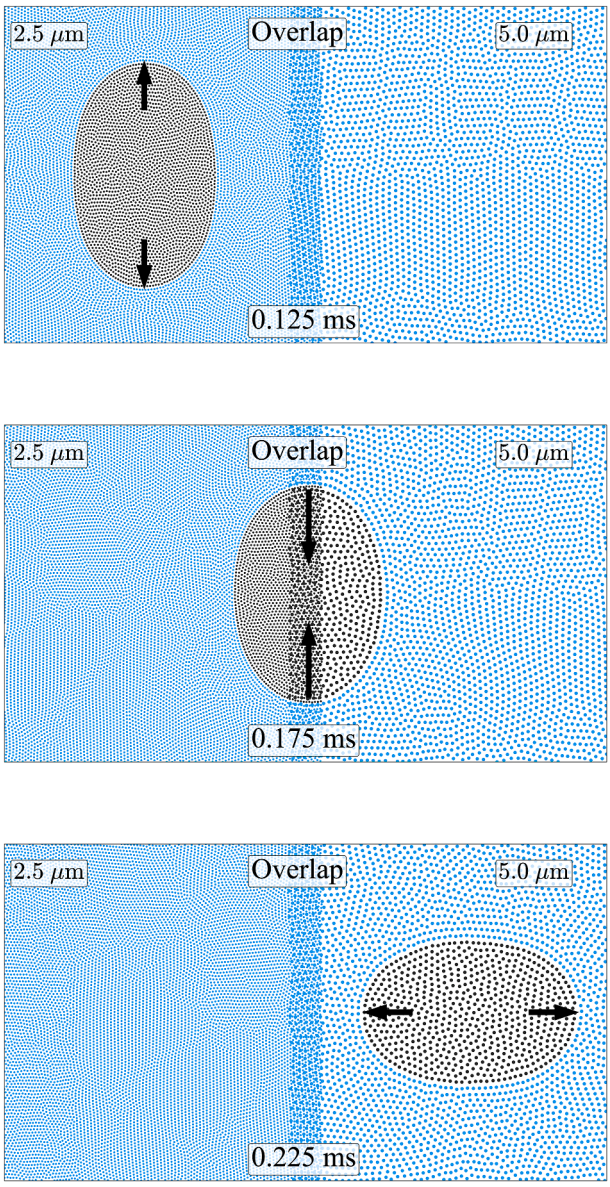

Fig. 28. Passing of oscillating droplet through transition zone at the area of interest (AOI). Only regular particles are visible.

The movement through the transition region is depicted in Fig. 28 by three snapshots taken at different time instances. At 0.175 ms the droplet is past its maximum extension in y-direction and starts to contract. At this time instance, the droplet volume is represented by both, the refined as well as the coarse particles. It is evident, that the transition process does not cause any deformation of the droplet interface during the oscillation. After successfully passing the transition zone, the droplet continues with its expected oscillation, cf. at 0.225 ms in Fig. 28.

In Fig. 29, the displacement amplitude of the droplet is plotted. The metric chosen is the displacement of the barycenter of only the upper half of the droplet. The time instance when the droplet passes through the transition zone is highlighted by the hatched area. For this comparison, the overlap region was extended to entirely cover the droplet. This is necessary to ease the extraction of a continuous displacement curve, as justified in Appendix B. Therefore, the time instance of the droplet leaving the transition zone is different compared to that of the previous discussion. However, the oscillation period is not affected. In general, an overlap of this size is not necessary as was shown previously (cf. Fig. 28). For comparison, the solutions predicted with uniform particle sizes are given. The predicted droplet oscillations are almost identical for all three finer predictions (cf. Fig. 29 Left). Only small deviations which are significantly smaller then the minimal resolution of $dx_{fine} = 2.5\,\mu m$ are visible. For the coarser resolutions (cf. Fig. 29 Right), a stronger dependence on resolution becomes evident. The uniform prediction with $dx_{coarse} = 10.0\,\mu m$ fails to capture the reduction of oscillation amplitude over time, which is also partly visible in the 5.0/10.0 MR case. At this resolution, however, the

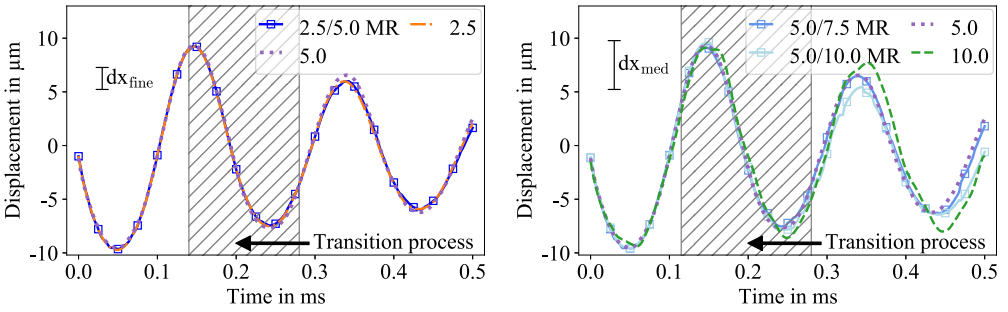

Fig. 29. Comparison of droplet oscillations at different resolutions. The amplitude is the displacement of the barycenter of the top half of the droplet. Left: Finer resolutions. Right: Coarser resolutions.

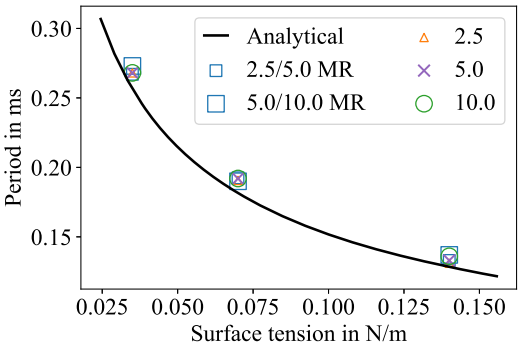

Fig. 30. Comparison of oscillation periods obtained for uniform and multi-resolution simulations.

droplet consist of only 158 particles, corresponding to roughly 15 particles across its diameter. In the 5.0/7.5 MR case, this improves, with the droplet comprising 277 particles in the coarse stage. It is evident that the phase interface remains intact after the transition and the droplet continues its oscillation, regardless of the resolution. The capability of restricting the refinement zone to the area of focus and still obtain data from liquid fragments downstream of the refinement zone is clearly demonstrated.

The predictions presented previously are now repeated to prove the reliability of the model over a wide range of surface tension values. By theory, in 2D the oscillation period of the nth mode is given by Rayleigh [62]:

$$\tau = 2\pi\sqrt{\frac{R^3\rho}{(n^3-n)\sigma}}. \tag{30}$$

The variations of the oscillating periods by modifying the surface tension for a single resolution model and the multi-resolution model are depicted in Fig. 30, along with the theoretical duration. Overall, all resolutions are capable of predicting the oscillation behavior. In order to counteract the change of oscillation mode and to avoid breakup of the droplet that occurs due to an excessive initial oscillation amplitude with decreasing surface tension, in cases of $\sigma = 0.035\,\mathrm{N\,m^{-1}}$, the value for U_0 was reduced to $1.25\,\mathrm{m\,s^{-1}}$. Negligible deviations are evident. Due to the fixed position of the derefinement zone, the constant mean velocity of the gas and droplet and the different oscillation periods, the droplet moves across regions of different resolution levels between different phases of its oscillation. Contracting in y-direction for $\sigma = 0.07\,\mathrm{N\,m^{-1}}$ (cf. Fig. 28) or expanding in x-direction for another value of σ. However, the shape of the droplet and direction of the droplets movement does not have an effect on the result.

4.5. Planar atomization

As a final highlight, the framework is applied to a scenario close to practical use. The multi-resolution framework was originally developed to support the prediction of airblast atomization. In this process, fuel is typically introduced onto a so-called prefilmer, where it is subjected to a much faster air stream. The resulting interaction leads to the breakup of the liquid film into fragments and droplets. To facilitate experimental investigations of airblast atomization, a simplified generic atomizer was developed and studied by Gepperth et al. [63,64,65], commonly referred to as the Gepperth prefilmer. This setup has also been investigated numerically by Braun et al. [10], Warncke et al. [66], Wetherell and Garmory [67]. A sketch of the geometry of the atomizer is shown in Fig. 31.

At this stage, comparability with uniform-resolution simulations remains important for a proper assessment of the multi-resolution framework. Therefore, the computational domain is restricted to the vicinity of the atomizing edge, located at the downstream end of the prefilmer. This is a standard approach for simulations of primary breakup [10,66] and also enables the generation of reference results with uniform resolutions. The total domain length is $l_{\mathrm{domain}} = 10\,\mathrm{mm}$, of which the prefilmer extends $l_{\mathrm{p}} = 4\,\mathrm{mm}$. Both inlets have a height of $h_{\mathrm{inlet}} = 4\,\mathrm{mm}$. The prefilmer thickness at the atomizing edge is $h_{\mathrm{a}} = 230\,\mu\mathrm{m}$ with a trailing-edge angle of $\alpha = 4.29°$. The liquid fuel film enters the domain via a block profile of height $h_{\mathrm{f}} = 100\,\mu\mathrm{m}$ and velocity $U_l = 0.5\,\mathrm{m\,s^{-1}}$. The free-stream gas

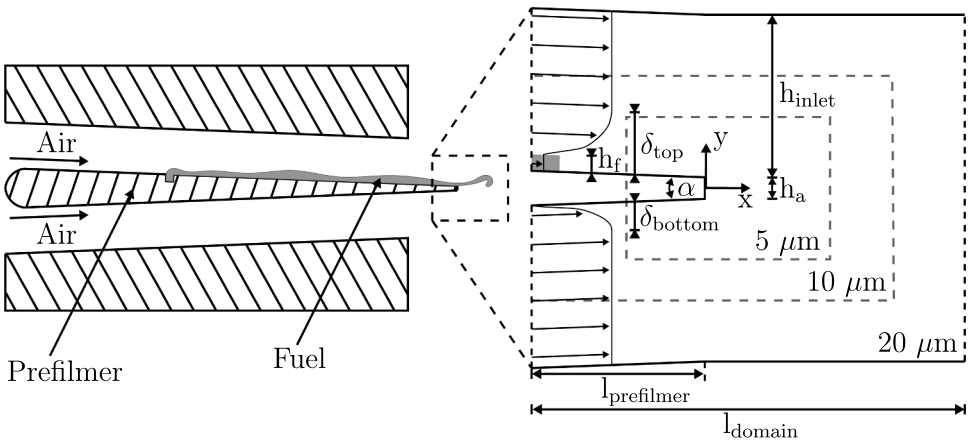

Fig. 31. Sketch of the Gepperth prefilmer (left) and the computational domain (right).

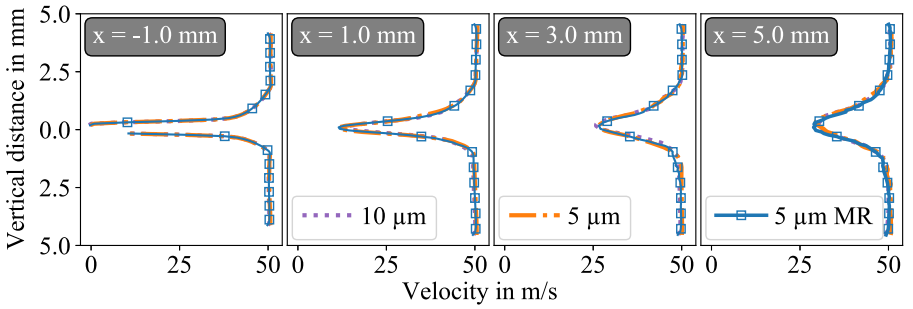

Fig. 32. Velocity profiles at different horizontal positions.

velocity is $U_g = 50\,\mathrm{m\,s^{-1}}$. Boundary layers on the upper and lower sides of the prefilmer are $\delta_{top} = 1.6\,\mathrm{mm}$ and $\delta_{bottom} = 0.8\,\mathrm{mm}$, respectively, consistent with the boundary-layer growth caused by liquid–gas interaction [67]. Gas inflow profiles follow a 1/7th power law.

The material parameters are: gas density $\rho_g = 1.19\,\mathrm{kg\,m^{-3}}$, liquid density $\rho_l = 770\,\mathrm{kg\,m^{-3}}$, viscosities $\mu_g = 0.018\,\mathrm{mPa\,s^{-1}}$ and $\mu_l = 1.56\,\mathrm{mPa\,s^{-1}}$, and surface tension $\sigma = 0.0275\,\mathrm{N\,m^{-1}}$. Artificial sound speeds are set to $c_g = 250\,\mathrm{m\,s^{-1}}$ for the gas and $c_l = 25\,\mathrm{m\,s^{-1}}$ for the liquid.

Three simulations are conducted: two uniform predictions with resolutions of 10 µm and 5 µm, and one multi-resolution case with refinement from 20 µm to 10 µm and 5 µm. The positioning of the zones of higher resolution is given by $x_{10\mu m} \in [\text{-}\infty,\ 4.5\,\mathrm{mm}]$ and $y_{10\mu m} \in [-2.25\,\mathrm{mm},\ 2.25\,\mathrm{mm}]$. A further refinement to 5 µm is then applied in the confined area $x_{5\mu m} \in [-1.0\,\mathrm{mm},\ 2.75\,\mathrm{mm}]$ and $y_{5\mu m} \in [-1.75\,\mathrm{mm},\ 1.75\,\mathrm{mm}]$. The total simulated physical time amounts to 50 ms.

In Fig. 32, averaged velocity profiles across the vertical position for multiple axial positions are depicted. The overall agreement is very good. Marginal differences are visible in the wake of the prefilming edge, where the gas flow is dominated by the primary breakup, the resulting spray cone width or the size of the liquid fragments. It is clear, that 10 µm is sufficient for the prediction of the gas flow.

In Fig. 33, breakup sequences at three different resolutions are shown. The breakup corresponds to the 2D analogue of a bubble breakup in 3D. Initially, a ligament is stretched beyond the atomizing edge (t_0), where it interacts with the lower air channel. The airflow penetrates into the emerging cavity and inflates the liquid ligament (t_1). During this stage, the ligament continues to elongate and thin (t_2). Eventually, when the resolution can no longer resolve the ongoing elongation and thinning, the bubble ruptures (t_3). As a result, the coarsest resolution of 10 µm exhibits the smallest gain in spatial extent from t_1 to t_3. The sudden upward or downward movement of the ligament during the elongation stage, caused by interaction with the gas flow, is referred to as flapping. This flapping motion is also suppressed in the 10 µm case due to the premature breakup.

The sequences are taken from different time instants and are therefore uncorrelated. Given the highly chaotic nature of atomization, driven by multiple instabilities and turbulent interactions with the liquid film, a perfect one-to-one correspondence between such sequences should not be expected, and direct comparisons must be made with caution. Over the total simulation time of 50 ms, only one breakup event of this kind was observed in the 10 µm case, emphasizing the need for higher resolution to reliably capture the breakup process, even though the resolution appeared sufficient for predicting the gas flow. By contrast, the uniform 5 µm simulation shows good agreement with the multi-resolution variant, both in ligament shape and size as well as in the gain of spatial extent.

In Fig. 34, the diameter–velocity clouds are shown for the three resolutions. Droplet characteristics are evaluated within a measurement volume located 1.0 mm downstream of the atomizing edge. Equivalent droplet diameters $\overline{D}$ are defined as the diameter

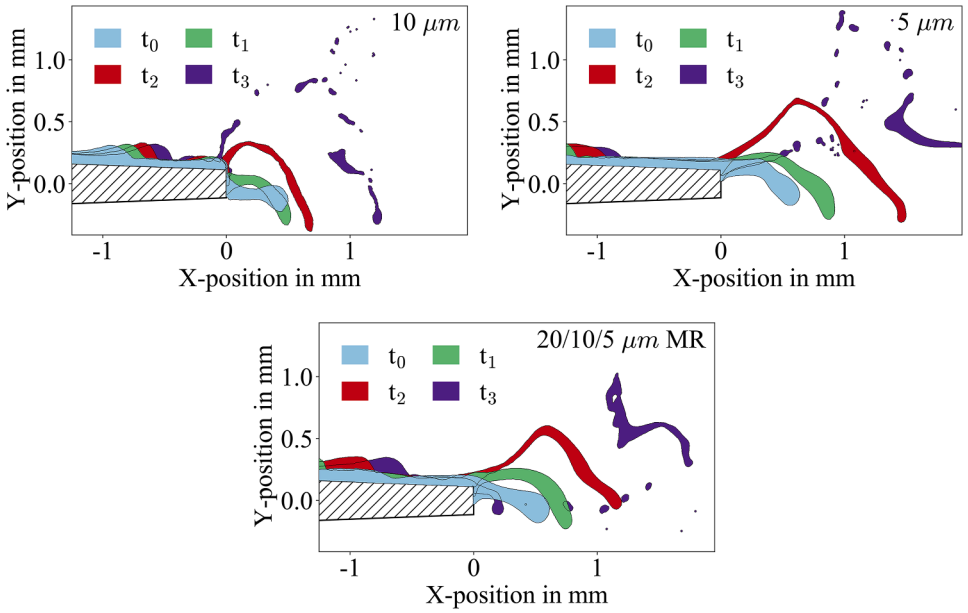

Fig. 33. Breakup sequences for three resolutions: uniform 10 µm, uniform 5 µm, and the multi-resolution variant 20/10/5 µm. The process represents the 2D analogue of a bubble breakup in 3D. Since the depicted breakup events are taken from different time instants, they are uncorrelated.

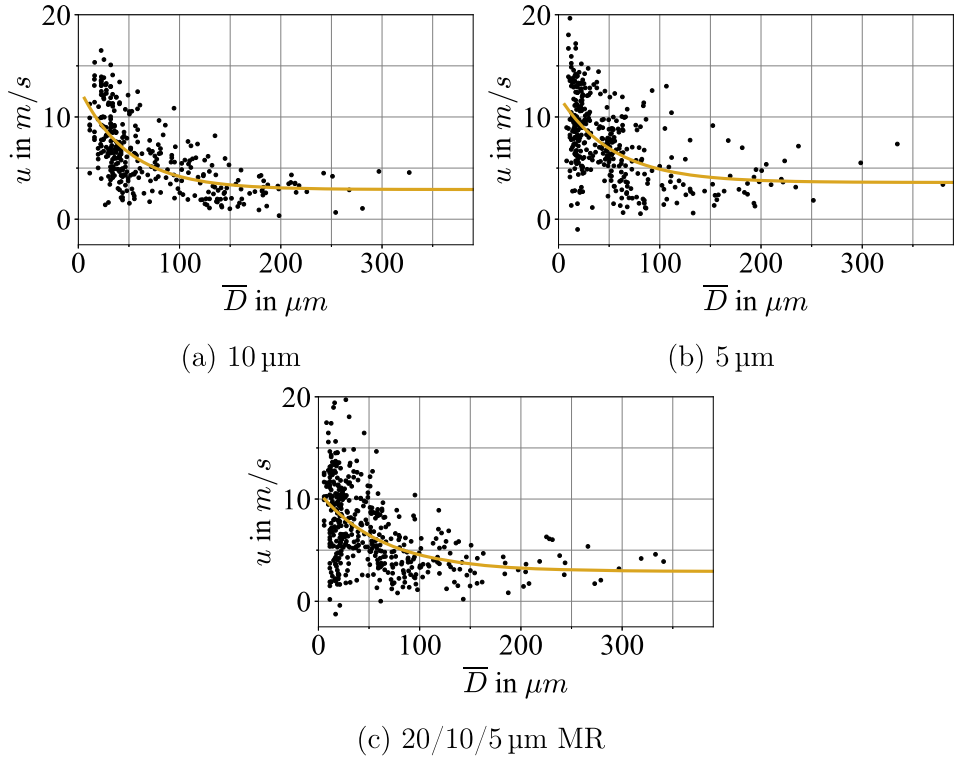

Fig. 34. Bivariate distribution of equivalent droplet diameters and velocities. The orange curve corresponds to the least-square fit.

of a spherical droplet with the same volume, allowing ligaments and fragments of arbitrary shape to be treated as droplets. Liquid clusters containing fewer than four particles were considered underresolved and discarded. As the resolution increases, the fraction of underresolved liquid volume generally decreases. Each simulation yielded between 350 and 450 droplets, with the fewest occurring in the 10 µm case. The bivariate distributions also include a least-squares fit of the averaged correlation [14].

The same trends are observed across all three resolutions: larger droplets tend to move more slowly, and the spread in possible velocities decreases accordingly. In the coarsest 10 µm case, the flapping motion is noticeably suppressed, leading to a reduced velocity

spread (cf. Fig. 34(a)). In the uniform 5 μm simulation (cf. Fig. 34(b)), a few outliers with larger diameters ($\overline{D} \geq 100\,\mu\text{m}$) and unusually high velocities slightly raise the averaged correlation fit. Longer simulation times and a larger number of droplets would be required to confirm this statistically. Nevertheless, the overall trends remain consistent across resolutions.

The multi-resolution simulation 20/10/5 μm MR comprises 0.93 million particles, compared to 3.28 million in the uniform 5 μm case and 0.83 million in the uniform 10 μm case. Using the multi-resolution approach, a speed-up of 3.15 was achieved relative to the finest uniform simulation, reducing the computational cost from 41,000 CPUh to 13,000 CPUh. This demonstrates that the multi-resolution framework is applicable to realistic atomizer scenarios, while effectively reducing computational cost and allowing larger portions of the geometry to be simulated.

5. Conclusion

Currently, multi-resolution SPH schemes for multi-phase flows are considered a Grand Challenge. In this work, we developed a new multi-resolution framework for multi-phase flow, based on a domain-decomposition strategy and by additionally incorporating techniques known from the treatment of boundary conditions. Our framework involves continuous mass insertion and deletion at the resolution interface and employs a state-of-the-art transport-velocity scheme and additional interface reconstruction for particles in the inter-resolution transition zone.

We validated the multi-resolution model by different benchmarks: a lid-driven cavity, a laminar Taylor–Green flow, a Kelvin–Helmholtz instability and an oscillating droplet. Finally, the model was demonstrated in an application near atomizer scenario. The model successfully replicated the reference results obtained with uniform resolutions and demonstrated its ability to handle single- and multi-phase flows. The model is capable of advecting the phase interface from one resolution level to the next. The ability to restrict the finest resolution only to the region of interest without influencing the phase interface is evident and will give significant advantages concerning computing effort. Using the multi-resolution framework, numerical results of the same quality can be obtained at lower computational costs. Multi-phase flows exist that exhibit physical phenomena both similar to and different from those demonstrated in this study. In future work, this framework will be extended to other realistic multi-phase flow scenarios, as well as to industrial applications such as 3D fuel nozzles.

CRediT authorship contribution statement

Niklas Bürkle: Writing – original draft, Visualization, Validation, Software, Methodology, Investigation, Formal analysis, Data curation; **Markus Wicker:** Writing – review & editing, Software, Methodology; **Max Okraschevski:** Writing – review & editing, Software; **Rainer Koch:** Writing – review & editing, Supervision, Resources, Project administration, Funding acquisition, Conceptualization; **Hans-Jörg Bauer:** Supervision, Resources, Project administration, Funding acquisition, Conceptualization.

Data availability

Data will be made available on request.

Declaration of competing interest

The authors declare that they have no known competing financial interests or personal relationships that could have appeared to influence the work reported in this paper.

Acknowledgment

The authors acknowledge funding by the German Federal Ministry for Economic Affairs and Energy (BMWI) and Rolls-Royce Deutschland Ltd. & Co. KG within the framework of research program Luftfahrtforschungsprogramm 5 (Project no. 20T1702). We acknowledge support by the KIT-Publication Fund of the Karlsruhe Institute of Technology. The authors acknowledge support by the state of Baden-Württemberg through bwHPC.

Appendix A. Kernels

For the previously discussed 2D simulations, the Wendland C4 kernel

$$W(q) = \frac{3}{1024\pi h^2} \begin{cases} (2-q)^6\,(35q^2+36q+12) & q \leq 2, \\ 0 & q > 2, \end{cases} \tag{A.1}$$

as well as the quintic spline kernel

$$W(q) = \frac{7}{478\pi h^2} \begin{cases} (3-q)^5 - 6(2-q)^5 + 15(1-q)^5 & q \leq 1, \\ (3-q)^5 - 6(2-q)^5 & 1 < q \leq 2, \\ (3-q)^5 & 1 \leq q \leq 2, \\ 0 & q > 3, \end{cases} \tag{A.2}$$

have been applied, using $q = r_{ij}/h$.

Appendix B. Overlap extension

The barycenter of the top half of a spherical, non-oscillating object undergoes a displacement when the object moves through a transition zone. This is illustrated in Fig. B.35. In order to avoid this effect, the overlap is extended until the droplet fits into the overlap. The oscillation amplitudes for each resolution level are evaluated independently. Subsequently the trajectories of the oscillation amplitudes are connected.

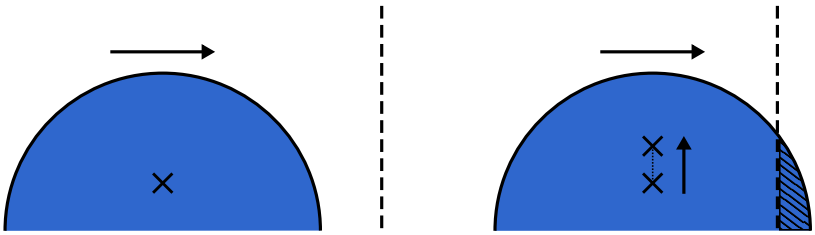

Fig. B.35. Displacement of the barycenter of a solid hemisphere due to the partial transition.

References

[1] J.J. Monaghan, A. Kocharyan, SPH simulation of multi-phase flow, Comput. Phys. Commun. 87 (1–2) (1995) 225–235. https://doi.org/10.1016/0010-4655(94)00174-z

[2] X.Y. Hu, N.A. Adams, A multi-phase SPH method for macroscopic and mesoscopic flows, J. Comput. Phys. 213 (2) (2006) 844–861. https://doi.org/10.1016/j.jcp.2005.09.001

[3] M.S. Shadloo, G. Oger, D. Le Touzé, Smoothed particle hydrodynamics method for fluid flows, towards industrial applications: motivations, current state, and challenges, Comput. Fluids 136 (2016) 11–34. https://doi.org/10.1016/j.compfluid.2016.05.029

[4] M. Luo, C.G. Koh, M. Gao, W. Bai, A particle method for two-phase flows with large density difference, Int. J. Numer. Methods Eng. 103 (4) (2015) 235–255. https://doi.org/10.1002/nme.4884

[5] Z.-B. Wang, R. Chen, H. Wang, Q. Liao, X. Zhu, S.-Z. Li, An overview of smoothed particle hydrodynamics for simulating multiphase flow, Appl. Math. Model. 40 (23–24) (2016) 9625–9655. https://doi.org/10.1016/j.apm.2016.06.030

[6] M. Luo, C.G. Koh, W. Bai, M. Gao, A particle method for two-phase flows with compressible air pocket: CPM for two-phase flows with compressible air pocket, Int. J. Numer. Methods Eng. 108 (7) (2016) 695–721. https://doi.org/10.1002/nme.5230

[7] T. Ye, D. Pan, C. Huang, M. Liu, Smoothed particle hydrodynamics (SPH) for complex fluid flows: recent developments in methodology and applications, Phys. Fluids 31 (1) (2019). https://doi.org/10.1063/1.5068697

[8] X.-S. Guan, P.-N. Sun, H.-G. Lyu, N.-N. Liu, Y.-X. Peng, X.-T. Huang, Y. Xu, Research progress of SPH simulations for complex multiphase flows in ocean engineering, Energies 15 (23) (2022) 9000. https://doi.org/10.3390/en15239000

[9] S. Braun, R. Koch, H.-J. Bauer, Smoothed particle hydrodynamics for numerical predictions of primary atomization, in: High Performance Computing in Science and Engineering '16, Springer International Publishing, 2016, pp. 321–336. https://doi.org/10.1007/978-3-319-47066-5_22

[10] S. Braun, L. Wieth, S. Holz, T.F. Dauch, M.C. Keller, G. Chaussonnet, S. Gepperth, R. Koch, H.-J. Bauer, Numerical prediction of air-assisted primary atomization using smoothed particle hydrodynamics, Int. J. Multiph. Flow 114 (2019) 303–315. https://doi.org/10.1016/j.ijmultiphaseflow.2019.03.008

[11] G. Chaussonnet, S. Braun, T. Dauch, M. Keller, A. Sänger, T. Jakobs, R. Koch, T. Kolb, H.-J. Bauer, Toward the development of a virtual spray test-rig using the smoothed particle hydrodynamics method, Comput. Fluids 180 (2019) 68–81. https://doi.org/10.1016/j.compfluid.2019.01.010

[12] G. Chaussonnet, T. Dauch, M. Keller, M. Okraschevski, C. Ates, C. Schwitzke, R. Koch, H.J. Bauer, Progress in the smoothed particle hydrodynamics method to simulate and post-process numerical simulations of annular airblast atomizers, Flow, Turbul. Combust. 105 (4) (2020) 1119–1147. https://doi.org/10.1007/s10494-020-00174-6

[13] T. Dauch, G. Chaussonnet, M. Keller, M. Okraschevski, C. Ates, R. Koch, H.-J. Bauer, 3D Predictions of the Primary Breakup of Fuel in Spray Nozzles for Aero Engines, Springer International Publishing, 2021, pp. 419–433. https://doi.org/10.1007/978-3-030-80602-6_27

[14] M. Okraschevski, L.C.C. Mesquita, R. Koch, E. Mastorakos, H.-J. Bauer, A numerical study of aero engine sub-idle operation: from a realistic representation of spray injection to detailed chemistry LES-CMC, Flow, Turbul. Combust. 111 (2) (2023) 493–530. https://doi.org/10.1007/s10494-023-00443-0

[15] R. Koch, S. Braun, L. Wieth, G. Chaussonnet, T. Dauch, H.-J. Bauer, Prediction of primary atomization using smoothed particle hydrodynamics, Eur. J. Mech. - B/Fluids 61 (2017) 271–278. https://doi.org/10.1016/j.euromechflu.2016.10.007

[16] R. Vacondio, C. Altomare, M. De Leffe, X. Hu, D. Le Touzé, S. Lind, J.-C. Marongiu, S. Marrone, B.D. Rogers, A. Souto-Iglesias, Grand challenges for smoothed particle hydrodynamics numerical schemes, Comput. Part. Mech. 8 (3) (2020) 575–588. https://doi.org/10.1007/s40571-020-00354-1

[17] L. Hernquist, N. Katz, TREESPH—A Unification of SPH with the hierarchical tree method, Astrophys. J. Suppl. Ser. 70 (1989) 419. https://doi.org/10.1086/191344

[18] J. Feldman, J. Bonet, Dynamic refinement and boundary contact forces in SPH with applications in fluid flow problems, Int. J. Numer. Methods Eng. 72 (3) (2007) 295–324. https://doi.org/10.1002/nme.2010

[19] Y.R. López, D. Roose, C.R. Morfa, Dynamic particle refinement in SPH: application to free surface flow and non-cohesive soil simulations, Comput. Mech. 51 (5) (2012) 731–741. https://doi.org/10.1007/s00466-012-0748-0

[20] R. Vacondio, B.D. Rogers, P.K. Stansby, P. Mignosa, J. Feldman, Variable resolution for SPH: a dynamic particle coalescing and splitting scheme, Comput. Methods Appl. Mech. Eng. 256 (2013) 132–148. https://doi.org/10.1016/j.cma.2012.12.014

[21] D.A. Barcarolo, D.L. Touzé, G. Oger, F. de Vuyst, Adaptive particle refinement and derefinement applied to the smoothed particle hydrodynamics method, J. Comput. Phys. 273 (2014) 640–657. https://doi.org/10.1016/j.jcp.2014.05.040

[22] R. Winchenbach, A. Kolb, Optimized refinement for spatially adaptive SPH, ACM Trans. Graph. 40 (1) (2021) 1–15. https://doi.org/10.1145/3363555

[23] X. Bian, Z. Li, G.E. Karniadakis, Multi-resolution flow simulations by smoothed particle hydrodynamics via domain decomposition, J. Comput. Phys. 297 (2015) 132–155. https://doi.org/10.1016/j.jcp.2015.04.044

[24] L. Chiron, G. Oger, M. de Leffe, D.L. Touzé, Analysis and improvements of adaptive particle refinement (APR) through CPU time, accuracy and robustness considerations, J. Comput. Phys. 354 (2018) 552–575. https://doi.org/10.1016/j.jcp.2017.10.041

[25] F. Ricci, R. Vacondio, A. Tafuni, Multiscale smoothed particle hydrodynamics based on a domain-decomposition strategy, Comput. Methods Appl. Mech. Eng. 418 (2024) 116500. https://doi.org/10.1016/j.cma.2023.116500

[26] F. Ricci, R. Vacondio, J.M. Domínguez, A. Tafuni, Three-dimensional variable resolution for multi-scale modeling in smoothed particle hydrodynamics, Comput. Phys. Commun. 313 (2025) 109609. https://doi.org/10.1016/j.cpc.2025.109609

[27] P.N. Sun, D.L. Touzé, A.M. Zhang, Study of a complex fluid-structure dam-breaking benchmark problem using a multi-phase SPH method with APR, Eng. Anal. Bound. Elem. 104 (2019) 240–258. https://doi.org/10.1016/j.enganabound.2019.03.033
[28] X. Yang, S.-C. Kong, Adaptive resolution for multiphase smoothed particle hydrodynamics, Comput. Phys. Commun. 239 (2019) 112–125. https://doi.org/10.1016/j.cpc.2019.01.002
[29] H. Cheng, Y. Liu, F.-R. Ming, P.-N. Sun, Investigation on the bouncing and coalescence behaviors of bubble pairs based on an improved APR-SPH method, Ocean Eng. 255 (2022) 111401. https://doi.org/10.1016/j.oceaneng.2022.111401
[30] J.J. Monaghan, Smoothed particle hydrodynamics, Annu. Rev. Astron. Astrophys. 30 (1) (1992) 543–574. https://doi.org/10.1146/annurev.aa.30.090192.002551
[31] M. Antuono, A. Colagrossi, S. Marrone, Numerical diffusive terms in weakly-compressible SPH schemes, Comput. Phys. Commun. 183 (12) (2012) 2570–2580. https://doi.org/10.1016/j.cpc.2012.07.006
[32] A. Colagrossi, M. Landrini, Numerical simulation of interfacial flows by smoothed particle hydrodynamics, J. Comput. Phys. 191 (2) (2003) 448–475. https://doi.org/10.1016/s0021-9991(03)00324-3
[33] K. Szewc, Smoothed particles hydrodynamics – the implementations of the incompressibility, Copernic. Lett. 1 (2010) 141–154. https://doi.org/10.12775/cl.2010.020
[34] S. Adami, X.Y. Hu, N.A. Adams, A new surface-tension formulation for multi-phase SPH using a reproducing divergence approximation, J. Comput. Phys. 229 (13) (2010) 5011–5021. https://doi.org/10.1016/j.jcp.2010.03.022
[35] P.N. Sun, A. Colagrossi, S. Marrone, M. Antuono, A.M. Zhang, Multi-resolution delta-plus-SPH with tensile instability control: towards high Reynolds number flows, Comput. Phys. Commun. 224 (2018) 63–80. https://doi.org/https://doi.org/10.1016/j.cpc.2017.11.016
[36] P.G. Tait, Report on Some of the Physical Properties of Fresh Water and of Sea Water, Report on the scientific results of the voyage of the H.M.S. Challenger during the years 1873-76: Physics and Chemistry, Johnson Reprint Corporation, 1965.
[37] G.R. Liu, M.B. Liu, Smoothed Particle Hydrodynamics, World Scientific, 2003. https://doi.org/10.1142/5340
[38] W. Dehnen, H. Aly, Improving convergence in smoothed particle hydrodynamics simulations without pairing instability, Mon. Not. R. Astron. Soc. 425 (2) (2012) 1068–1082. https://doi.org/10.1111/j.1365-2966.2012.21439.x
[39] M. Okraschevski, N. Buerkle, R. Koch, H.J. Bauer, Smoothed particle hydrodynamics physically reconsidered: the relation to explicit large eddy simulation and the issue of particle duality, Phys. Fluids 34 (11) (2022). https://doi.org/10.1063/5.0105104
[40] M. Okraschevski, Über den Zusammenhang von Large Eddy Simulation und Smoothed Particle Hydrodynamics, Dissertation, Institut für Thermische Strömungsmaschinen, Karlsruher Institut für Technologie (KIT), 2024. https://doi.org/10.5445/IR/1000170106
[41] M. Antuono, P.N. Sun, S. Marrone, A. Colagrossi, The delta-ALE-SPH model: an arbitrary Lagrangian–Eulerian framework for the delta-SPH model with particle shifting technique, Comput. Fluids 216 (2021) 104806. https://doi.org/10.1016/j.compfluid.2020.104806
[42] C. Pilloton, P.N. Sun, X. Zhang, A. Colagrossi, Volume conservation issue within SPH models for long-time simulations of violent free-surface flows, Comput. Methods Appl. Mech. Eng. 419 (2024) 116640. https://doi.org/10.1016/j.cma.2023.116640
[43] J.P. Morris, A Study of the Stability Properties of SPH, 1995. https://doi.org/10.48550/ARXIV.ASTRO-PH/9503124
[44] S. Adami, X.Y. Hu, N.A. Adams, A transport-velocity formulation for smoothed particle hydrodynamics, J. Comput. Phys. 241 (2013) 292–307. https://doi.org/10.1016/j.jcp.2013.01.043
[45] S.J. Lind, R. Xu, P.K. Stansby, B.D. Rogers, Incompressible smoothed particle hydrodynamics for free-surface flows: a generalised diffusion-based algorithm for stability and validations for impulsive flows and propagating waves, J. Comput. Phys. 231 (4) (2012) 1499–1523. https://doi.org/10.1016/j.jcp.2011.10.027
[46] R. Xu, P. Stansby, D. Laurence, Accuracy and stability in incompressible SPH (ISPH) based on the projection method and a new approach, J. Comput. Phys. 228 (18) (2009) 6703–6725. https://doi.org/10.1016/j.jcp.2009.05.032
[47] A. Mokos, B.D. Rogers, P.K. Stansby, A multi-phase particle shifting algorithm for SPH simulations of violent hydrodynamics with a large number of particles, J. Hydraul. Res. 55 (2) (2016) 143–162. https://doi.org/10.1080/00221686.2016.1212944
[48] G. Oger, S. Marrone, D.L. Touzé, M. de Leffe, SPH accuracy improvement through the combination of a quasi-Lagrangian shifting transport velocity and consistent ALE formalisms, J. Comput. Phys. 313 (2016) 76–98. https://doi.org/10.1016/j.jcp.2016.02.039
[49] F. Ricci, R. Vacondio, A. Tafuni, Direct numerical simulation of three-dimensional isotropic turbulence with smoothed particle hydrodynamics, Phys. Fluids 35 (6) (2023). https://doi.org/10.1063/5.0152154
[50] M. Okraschevski, N. Bürkle, M. Wicker, R. Koch, H.-J. Bauer, Evidence on the incompatibility of modern SPH methods and eddy viscosity models for scale-resolved incompressible turbulence, 2025, (Under consideration for publication in J. Fluid Mech). https://doi.org/10.48550/ARXIV.2506.08538
[51] S. Marrone, A. Colagrossi, D. Le Touzé, G. Graziani, Fast free-surface detection and level-set function definition in SPH solvers, J. Comput. Phys. 229 (10) (2010) 3652–3663. https://doi.org/10.1016/j.jcp.2010.01.019
[52] X. Xu, P. Yu, A technique to remove the tensile instability in weakly compressible SPH, Comput. Mech. 62 (5) (2018) 963–990. https://doi.org/10.1007/s00466-018-1542-4
[53] N. Grenier, M. Antuono, A. Colagrossi, D.L. Touzé, B. Alessandrini, An Hamiltonian interface SPH formulation for multi-fluid and free surface flows, J. Comput. Phys. 228 (22) (2009) 8380–8393. https://doi.org/10.1016/j.jcp.2009.08.009
[54] D. Shepard, A two-dimensional interpolation function for irregularly-spaced data, in: Proceedings of the 1968 23rd ACM National Conference, ACM Press, 1968. https://doi.org/10.1145/800186.810616
[55] B. Werdelmann, R. Koch, W. Krebs, H.-J. Bauer, An approach for permeable boundary conditions in SPH, J. Comput. Phys. 444 (2021) 110562. https://doi.org/10.1016/j.jcp.2021.110562
[56] A. Leroy, D. Violeau, M. Ferrand, L. Fratter, A. Joly, A new open boundary formulation for incompressible SPH, Comput. Math. Appl. 72 (9) (2016) 2417–2432. https://doi.org/10.1016/j.camwa.2016.09.008
[57] U. Ghia, K.N. Ghia, C.T. Shin, High-Re solutions for incompressible flow using the Navier–Stokes equations and a multigrid method, J. Comput. Phys. 48 (3) (1982) 387–411. https://doi.org/10.1016/0021-9991(82)90058-4
[58] A. Bauer, V. Springel, Subsonic turbulence in smoothed particle hydrodynamics and moving-mesh simulations, Mon. Not. R. Astron. Soc. 423 (3) (2012) 2558–2578. https://doi.org/10.1111/j.1365-2966.2012.21058.x
[59] D. Lecoanet, M. McCourt, E. Quataert, K.J. Burns, G.M. Vasil, J.S. Oishi, B.P. Brown, J.M. Stone, R.M. O'Leary, A validated non-linear Kelvin–Helmholtz benchmark for numerical hydrodynamics, Mon. Not. R. Astron. Soc. 455 (4) (2015) 4274–4288. https://doi.org/10.1093/mnras/stv2564
[60] T.S. Tricco, The Kelvin–Helmholtz instability and smoothed particle hydrodynamics, Mon. Not. R. Astron. Soc. 488 (4) (2019) 5210–5224. https://doi.org/10.1093/mnras/stz2042
[61] N. Ashgriz (Ed.), Handbook of Atomization and Sprays, Springer US, 2011. https://doi.org/10.1007/978-1-4419-7264-4
[62] Rayleigh, VI. On the capillary phenomena of jets, Proc. R. Soc. Lond. 29 (196–199) (1879) 71–97. https://doi.org/10.1098/rspl.1879.0015
[63] S. Gepperth, D. Guildenbecher, R. Koch, H.-J. Bauer, Pre-filming primary atomization: experiments and modeling, in: 23rd European Conference on Liquid Atomization and Spray Systems (ILASS-Europe 2010), Brno, Czech Republic, September, 2010, pp. 6–8.
[64] S. Gepperth, A. Müller, R. Koch, H.-J. Bauer, Ligament and droplet characteristics in prefilming airblast atomization, in: 12th Triennial International Conference on Liquid Atomization and Spray Systems (ICLASS), Heidelberg, Germany, September, 2012, pp. 2–6.
[65] S. Gepperth, E. Bärow, R. Koch, H.-J. Bauer, Primary atomization of prefilming airblast nozzles: experimental studies using advanced image processing techniques, in: 26th Annual Conference on Liquid Atomization and Spray Systems (ILASS-Europe 2014), Bremen, Germany, September, 2014, pp. 8–10.
[66] K. Warncke, S. Gepperth, B. Sauer, A. Sadiki, J. Janicka, R. Koch, H.J. Bauer, Experimental and numerical investigation of the primary breakup of an airblasted liquid sheet, Int. J. Multiph. Flow 91 (2017) 208–224. https://doi.org/10.1016/j.ijmultiphaseflow.2016.12.010
[67] J.R.J. Wetherell, A. Garmory, Air-film coupling in prefilming airblast atomisers and the implications for subsequent atomisation, Flow, Turbul. Combust. 113 (4) (2024) 975–1002. https://doi.org/10.1007/s10494-024-00565-z